Uncovering the spatial heterogeneity of Ediacaran carbon cycling

Chao Li[1*], Dalton S. Hardisty[2,3], Genming Luo[1], Junhua Huang[4], Thomas J. Algeo[1,4,5], Meng Cheng[1], Wei Shi[1], Zhihui An[6], Jinnan Tong[1], Shucheng Xie[1], Nianzhi Jiao[7], Timothy W. Lyons[3]

[1] *State Key Laboratory of Biogeology and Environmental Geology, China University of Geosciences, Wuhan 430074, China*

[2] *Department of Geology and Geophysics,* Woods Hole Oceanographic Institution, Woods Hole, MA 02543-1050, USA

[3] *Department of Earth Sciences, University of California, Riverside, CA 92521, USA*

[4] *State Key Laboratory of Geological Processes and Mineral Resources, China University of Geosciences, Wuhan 430074, China*

[5] *Department of Geology, University of Cincinnati, Cincinnati, OH 45221, U.S.A.*

[6] *Faculty of Earth Sciences, China University of Geosciences, Wuhan 430074, China*

[7] *State Key Laboratory of Marine Environmental Science, Xiamen University, Xiamen 361005, China*

[*] *Corresponding author. Tel: +86-27-67883606; E-mail address: chaoli@cug.edu.cn*

ABSTRACT

Records of the Ediacaran carbon cycle (635 to 541 million years ago) include the Shuram excursion (SE), the largest negative carbonate-carbon isotope excursion in Earth history (down to -12 ‰). The nature of this excursion remains enigmatic given the difficulties of interpreting a perceived extreme global decrease in the $\delta^{13}C$ of seawater dissolved inorganic carbon (DIC). Here, we present carbonate and organic carbon isotope ($\delta^{13}C_{carb}$ and $\delta^{13}C_{org}$) records from the Ediacaran Doushantuo Formation along a proximal-to-distal transect across the Yangtze Platform of South China as a test of the spatial variation of the SE. Contrary to expectations, our results show that the magnitude and morphology of this excursion and its relationship with coexisting $\delta^{13}C_{org}$ are highly heterogeneous across the platform. Integrated geochemical, mineralogical, petrographic, and stratigraphic evidence indicates that the SE is a primary marine signature. Data compilations demonstrate that the SE was also accompanied globally by parallel negative shifts of $\delta^{34}S$ of carbonate-associated sulfate (CAS) and increased $^{87}Sr/^{86}Sr$ ratio and coastal CAS concentration, suggesting elevated continental weathering and coastal marine sulfate concentration during the SE. In light of these observations, we propose a heterogeneous oxidation model to explain the high spatial heterogeneity of the SE and coexisting $\delta^{13}C_{org}$ records of the Doushantuo, with likely relevance to the SE in other regions. In this model, we infer continued marine redox stratification through the SE but with increased availability of oxidants (e.g., O_2 and sulfate) limited to marginal near-surface marine environments. Oxidation of limited spatiotemporal extent provides a mechanism to drive heterogeneous oxidation of

subsurface reduced carbon mostly in shelf areas. Regardless of the mechanism driving the SE, future models must consider the evidence for spatial heterogeneity in $\delta^{13}C$ presented in this study.

Keywords: Ediacaran carbon cycle, Doushantuo Formation, Shuram excursion, spatial heterogeneity, surface-ocean oxygenation

INTRODUCTION

The Ediacaran Period (635-541 million years ago or Ma) is characterized by a lack of global-scale glaciation (unlike the preceding Cryogenian Period), rising but perhaps still variable oxygen levels on the Earth's surface, and biological innovations culminating in innovation among early animals (Och & Shields-Zhou, 2012; Pecoits et al., 2012; Lyons et al., 2014; Droser & Gehling, 2015; Sahoo et al., 2016). The Ediacaran is also characterized by a series of major perturbations to the carbon cycle recorded globally in carbonate carbon isotope ($\delta^{13}C_{carb}$) profiles (Grotzinger et al., 2011). Carbonates of the mid-Ediacaran Shuram excursion (SE) yield a decrease in $\delta^{13}C$ values to as low as –12 ‰, placing it among the most negative excursions in Earth history. These values are appreciably more negative than the mantle $\delta^{13}C$ of ca. –5 ‰, requiring major inputs of isotopically light carbon to the exogenic Earth system during the SE (Grotzinger et al., 2011). The SE is also characterized by a general lack of carbonate isotopic co-variation with co-occurring organic carbon ($\delta^{13}C_{org}$), which contrasts with conventional views of the carbon cycle wherein both $\delta^{13}C_{carb}$ and $\delta^{13}C_{org}$

67 are derived from the same seawater dissolved inorganic carbon (DIC) reservoir and co-vary
68 accordingly (Rothman et al., 2003). The unusual operation of the global carbon cycle during
69 the Ediacaran may hold a key to understanding the co-evolution of life and environments at
70 that time (Grotzinger et al., 2011).

71 Currently, two leading hypotheses have been proposed to explain the origin of the SE.
72 The first centers on a range of secondary alteration scenarios involving either meteoric waters
73 or burial diagenesis (e.g., Knauth and Kennedy, 2009; Derry, 2010a, b; Swart and Kennedy,
74 2012; Schrag et al., 2013). Indeed, sea level fluctuation and subsequent periodic sub-areal
75 carbonate platform exposures can yield widespread meteoric overprints (Swart and Kennedy,
76 2012). However, models based on secondary alteration, which is inherently a local process,
77 are still generally criticized as inconsistent with the global nature of the event (Grotzinger et
78 al., 2011). The second hypothesis invokes the oxidation of a massive ^{13}C-depleted dissolved
79 organic carbon (DOC) reservoir in the Ediacaran oceans during the global oxygenation of a
80 formerly anoxic deep ocean, which drove the isotopic composition of DIC ($\delta^{13}C_{DIC}$) in
81 seawater and, in turn, coeval $\delta^{13}C_{carb}$ to strongly negative values (e.g., Rothman et al., 2003;
82 Fike et al., 2006; Jiang et al., 2007; McFadden et al., 2008). In this model, the size of the
83 hypothesized DOC pool buffered the $\delta^{13}C_{org}$ record against isotopic change. However, the
84 DOC oxidation hypothesis has been challenged because of the extreme oxidant demand that
85 would have been required to drive $\delta^{13}C_{DIC}$ of the entire ocean to –12 ‰ during marine
86 ventilation (Bristow and Kennedy, 2008). More generally, the presence and nature of the
87 hypothesized DOC pool and the possible mechanisms behind its generation and maintenance
88 remain poorly known and highly debated.

Here, we shed important new light on interpreting the $\delta^{13}C$ records of the SE by investigating basin-scale spatial heterogeneity of the SE as recorded in the Ediacaran Doushantuo Formation along a proximal-to-distal transect across the Yangtze Platform of South China. Our results indicate a strong heterogeneity for the SE across the Yangtze Platform, which challenges the notion that the most extreme negative carbonate $\delta^{13}C$ values represent that of global seawater and suggests instead that the mechanism driving the excursion was spatially variable.

GEOLOGICAL SETTING AND STUDY SECTIONS

The Ediacaran Yangtze Platform in South China was a passive continental margin, which formed at ~820 Ma along the rifted southeastern margin of the Yangtze Block during breakup of the Rodinia supercontinent (Wang and Li, 2003). Paleogeographic reconstructions for the Ediacaran Yangtze Platform envisage shallow rimmed platform, slope, and basin environments along a northwest-southeast transect based on lateral variations in lithofacies and stratal thicknesses (Jiang et al. 2011; Fig. 1A). The Doushantuo Formation was deposited in shallow to deep waters on the Yangtze Platform (Fig. 1B) following the last Neoproterozoic global-scale glaciation—the Marinoan (or 'Nantuo' in South China) event (Fig. 2). Deposition of the Doushantuo Formation continued for ~84 Myr, spanning most of the Ediacaran Period, based on U-Pb ages of 635.2±0.6 Ma and 551.1±0.7 Ma derived from ash beds at its base and top (Condon et al., 2005). However, a slightly older age of ~560 Ma was recently suggested for the top of Doushnatuo Formation based on stratigraphic

correlation of the Miaohe Member of the Doushantuo Formation in the Yangtze Gorges area (An et al., 2015). The Doushantuo Formation is also known for its fossil animal embryos (Yin et al., 2007), macroscopic algae (Yuan et al., 2011), and abundant acritarchs (McFadden et al., 2008), marking milestones in eukaryotic evolution and, more generally, the historical march from simple to complex life (Xiao et al., 2014, and references therein).

Our samples of the Doushantuo Formation were collected at several locales: the inner-shelf Zhangcunping site (ZCP; drillcore-ZK312), the intra-shelf-basin of Jiulongwan (JLW; outcrop), and the upper-slope Siduping sections (SDP; outcrop). These sections contain abundant carbonate and represent a proximal-to-distal transect across the Yangtze Platform (Fig. 1), allowing us to investigate spatial variation of the SE. The JLW and SDP sections were previously studied for both $\delta^{13}C_{carb}$ and $\delta^{13}C_{org}$ (McFadden et al., 2008; Li et al., 2010; Jiang et al., 2010; Wang et al., 2016; see 'Samples' section), and their stratigraphic details were reported in McFadden et al (2008) and Wang et al. (2016). In light of this previous work, we focus on a description of the new ZCP section in this study and interpret those data within the broader context.

The ZCP ZK312 drill site is located in Duanjiang Village, Baokang County, Hubei Province. In this core, the Ediacaran Doushantuo Formation has a total thickness of ~138 m and can be subdivided into four lithostratigraphic members (Fig. 2A). Member I is a 2.91-m-thick cap carbonate that overlies Cryogenian glacial diamictites of the Nantuo Formation; it consists of light gray and thickly bedded microcrystalline dolostone with stromatactis-like cavities. Member II consists of four lithologic subunits: (1) Member IIa is a 12.99-m black shale containing phosphatic layers and nodules, mainly in its upper portion; (2)

Member IIb is a 14.48-m, thick-bedded, gray, microcrystalline dolostone; (3) Member IIc is a 21.28-m, thin-bedded, gray, microcrystalline dolostone containing phosphorite in its middle third; and (4) Member IId is a 26.24-m, thin-bedded, dark gray, microcrystalline dolostone containing large chert nodules. Previous studies of the Zhangcunping outcrops inferred an erosional surface between members IIb and IIc (Fig. 2A; Zhou et al., 2005; Liu et al., 2009; Zhu et al., 2007; 2013), but our field observations suggest otherwise because strata above and below this surface show similar lithologies and sedimentary structures. Member III is a 46.93-m, thin-to-medium-bedded, gray, microcrystalline dolostone containing thin intercalations of black shale in its middle portion and chert layers in its upper portion. Member IV is a 12.88-m, thin-bedded, dark gray, microcrystalline dolostone that is distinct from the overlying thick-bedded, light gray dolostone of the Hamajing Member of the Dengying Formation.

The microfossil assemblages from the Zhangcunping area were found mostly in chert nodules of the upper Member II (Zhang et al., 1986; Zhou et al., 2004, 2005; Liu et al., 2009). These assemblages contain cyanobacteria, multicellular algae, and acritarchs that are similar to silicified fossils from members II and III of the Doushantuo Formation in the Yangtze Gorges area (Liu et al., 2009). A zircon SHRIMP U-Pb age (614.0±7.6 Ma) was obtained from the bottom of the Member IIb at the Wanjiagou section in the Zhangcunping area (Liu et al., 2009).

STRATIGRAPHIC CORRELATION

155 The intra-shelf-basin of JLW and the upper-slope SDP section, as well as other sections
156 across the Yangtze Platform, can be correlated on the basis of distinctive marker beds—i.e.,
157 the basal cap carbonate of Member I and the black shale of Member IV, in combination with
158 other stratigraphic surfaces of regional extent (Jiang et al., 2011; Zhu et al., 2013; Wang et al.,
159 2016; Fig. 2). The new inner-shelf ZCP section of the present study fits readily into this
160 correlation framework (Fig. 2). First, the basal cap carbonate overlying the Nantuo glacial
161 diamictites at ZCP is equivalent to cap carbonates in the JLW and SDP sections. Second,
162 Member II of the Doushantuo Formation can be correlated regionally based on lithologic and
163 faunal characteristics. At ZCP, Member II consists of dark-colored black shale and limestone
164 containing acritarchs, multicellular algae-cyanobacteria fossils, and abundant chert nodules.
165 These features correspond to those seen in the JLW section (Liu et al., 2009), although JLW
166 contains a larger proportion of black shale (McFadden et al., 2008). The Member II/III
167 contact is characterized by similar, abrupt lithofacies changes in both sections—i.e., from
168 thin-bedded, dark gray, dolostone containing large chert nodules to medium-bedded, light
169 gray dolostone without chert nodules at ZCP, and from thin-bedded dolostone with
170 intercalated black shales to thick-bedded dolostone lacking black shale at JLW. These facies
171 shifts reflect a rapid shoaling at the base of Member III at both sites. Third, the Member
172 III/IV contact can be correlated between ZCP and JLW based on similar lithofacies changes
173 from thick-bedded, light gray dolostone containing chert layers to thin-bedded, dark gray
174 dolostone at ZCP, and from medium-bedded limestone with dolomite caps to black shales at
175 JLW, reflecting a rapid deepening at the base of Member IV at both sites. Finally, Member IV
176 is unconformably overlain by thick-bedded, medium gray dolostone of the Dengying

177 Formation at both sites. Small differences in lithology within correlative intervals of these
178 sections most likely reflect local variation in water depths, watermass circulation, and
179 siliciclastic inputs, but they do not obscure overall similarities in these stratigraphic
180 successions (Jiang et al., 2011; Zhu et al., 2007, 2013). The correlation framework of the
181 study sections offers a unique opportunity to explore the spatial variation of the SE and other
182 Ediacaran excursions.
183
184 # SAMPLES AND ANALYTICAL METHODS
185
186 ## Samples
187 A total of 386 sedimentary rock samples were collected for this study between July 2012
188 and December 2013 and analyzed for the isotopic composition of carbonate ($\delta^{13}C_{carb}$ and
189 $\delta^{18}O_{carb}$) and coexisting organic matter ($\delta^{13}C_{org}$) (see Table S1). These samples include 171
190 (all dolomite) from the ZCP section (ZK312 drillcore), 57 (33 dolomite, 24 limestone) from
191 the JLW section (outcrop), and 158 (all dolomite) from the SDP section avoiding the
192 olistostrome breccias (outcrop). The 57 JLW samples were collected with the goal of
193 providing a more complete record of the SE compared to those established in earlier studies
194 of the same section (McFadden et al., 2008; Li et al., 2010). For the outcrop sites, large fresh
195 blocks of rock (> 200 g) were collected, and any visibly weathered surfaces and diagenetic
196 veins or cements were removed. Each block was then cut into small pieces (~1 cm^3) in the
197 laboratory, and only those pieces with no visible weathering or veins were selected for

198 powdering. Samples were crushed to finer than 200 mesh using a Retsch RS200 vibratory
199 disc mill.
200
201 **Carbonate $\delta^{13}C$ and $\delta^{18}O$ analyses**
202 About 60 to 300 μg of sample powder were loaded into a vial after drying at 70°C for 24
203 hours in an argon atmosphere. The samples were then reacted with 100 % phosphoric acid
204 under a vacuum at 70°C for 220 seconds using a Kiel IV device. The resulting CO_2 was
205 subsequently introduced into a MAT 253 isotope ratio mass spectrometer (IRMS) for isotopic
206 measurements. Delta values were calibrated relative to international reference standard
207 NBS-19 ($\delta^{13}C$ = +1.95 ‰; $\delta^{18}O$ = –2.20 ‰) and Chinese national standard GBW04416 ($\delta^{13}C$
208 = +1.61±0.03 ‰; $\delta^{18}O$ = –1.59±0.11 ‰). Carbon and oxygen isotope data for carbonates are
209 reported relative to Vienna Pee Dee Belemnite (VPDB) with a precision of better than ±0.1 ‰
210 based on duplicate analyses of GBW04416 and the study samples.
211
212 **Organic $\delta^{13}C$ analysis**
213 An aliquot of sample powder (~5-30 g) was reacted with 6 M HCl to completion. The
214 decarbonated residue was rinsed with deionized water to neutral pH, then centrifuged and
215 freeze dried for 24 hours. Samples with low TOC contents were treated further with HF to
216 remove silicates before isotopic analysis. Organic $\delta^{13}C$ was measured online using a Flash EA
217 2000 interfaced with a MAT 253 IRMS and calibrated with the glycine ($\delta^{13}C$ = −33.3 ‰) and
218 collagen ($\delta^{13}C$ = −9.0 ‰) SIGMA standards. Results are reported relative to the VPDB
219 standard with a precision better than ±0.2 ‰ based on duplicate analyses of study samples.

220

221 **Analyses of abundance and $\delta^{34}S$ of carbonate-associated sulfate (CAS)**

222 An aliquot of sample powder (~20 to 50 g with total inorganic carbon content > 3%;
223 77 samples from JLW section) was washed in a 10% NaCl solution for 24 hours before
224 removing the supernatant. This step was repeated multiple times until there was no barite
225 ($BaSO_4$) precipitation from the supernatant when adding saturated $BaCl_2$ solution (~250g/L).
226 The residual powder was then treated with 4 M HCl until the reaction completed. The filtered
227 solution was treated with 125 mL saturated $BaCl_2$ to precipitate the target CAS as barite,
228 which was then filtered, dried, and weighed for calculating CAS concentration in the
229 carbonate fraction of original sample by correcting for the amount of insoluble material
230 (assuming that all of the dissolved material was pure carbonate). The collected barite was
231 mixed with excess V_2O_5 for online combustion, and resulting SO_2 was measured on a Thermo
232 Scientific Delta V Plus isotope ratio mass spectrometer coupled with a Flash elemental
233 analyzer for sulfur isotope composition of the CAS ($\delta^{34}S_{CAS}$). Sulfur isotope compositions are
234 expressed in standard δ-notation as permil (‰) deviation from the V-CDT international
235 standard with an analytical error of 0.2 ‰ (1σ) calculated from replicate analyses of IAEA
236 standards (NBS-127, IAEA-SO-5, IAEA-SO-6).

237

238 **Mn and Sr concentration analyses**

239 About 50 mg of dried sample powder were dissolved using a standard HNO_3-HF
240 digestion as described below. The digestion step included progressive acid treatments at
241 190°C in a 15 ml Teflon bomb equipped with a screw cap to which HNO_3-HF (1:1) and

242 HNO_3 were added sequentially until complete digestion was achieved. Distilled HNO_3 and
243 trace metal-grade HF reagents were used for all samples. Following an evaporation procedure
244 to remove concentrated acid, the sample was diluted with 2 % nitric acid. Elemental
245 concentrations were measured using either an Agilent 7700x inductively coupled plasma
246 mass spectrometer (ICP-MS) for Mn and Sr or a Thermo Fisher ICAP 7400 inductively
247 coupled plasma optical emission spectrometry (ICP-OES) for Mn. Analytical errors are better
248 than ±4.7 % for Mn and ±6.3 % for Sr based on duplicate analyses of four USGS standards
249 (BCR-2, AGV-2, BHVO-2, RGM-2) and one Chinese national standard (GSR5).
250
251 # RESULTS AND DISCUSSION
252
253 ## Spatial heterogeneity of $\delta^{13}C$ record across the Yangtze Platform
254 Our C isotope data, together with data from earlier investigations from the relevant
255 sections (JLW: McFadden et al., 2008; Li et al., 2010; SDP: Jiang et al., 2010), are compiled
256 in Fig. 2 and Table S1. A recently published C isotope profile for the SDP section (Wang et al.,
257 2016) shows stratigraphic trends that are quite similar to those in our dataset but with some
258 differences in vertical scaling attributable to independent field measurements (note: we show
259 only our dataset in Fig. 2).
260 Our integrated data from the intra-shelf-basin JLW site and upper-slope SDP sections
261 reveal three major negative $\delta^{13}C_{carb}$ excursions (EN1, EN2, and EN3; see below) separated by
262 two positive intervals (IP1 and IP2) with $\delta^{13}C_{carb}$ values of ca. +4 to +5 ‰ at each location
263 (Fig. 2; note: we define negative excursion in this study in terms of a decrease in $\delta^{13}C_{carb}$

values from the baseline of ca. +4 to +5 ‰ observed at all our sections). EN1 is associated with the basal cap carbonate (Member I), and EN2 and EN3 are associated with abrupt facies changes at the bases of Members III and IV, respectively (Fig. 2B-C; cf. McFadden et al., 2008; Li et al., 2010; Wang et al., 2016). In contrast, our new data from the inner-shelf ZCP section show four negative $\delta^{13}C_{carb}$ excursions (EN1-1, EN1-2, EN2, and EN3) separated by three positive intervals of ca. +5 ‰ (IP, IP1, and IP2; see Fig. 2A). EN1-1, EN2, and EN3 at ZCP can be correlated to the equivalent excursions at JLW and SDP based on independent stratigraphic correlations described above under 'Stratigraphic correlation,' but the EN1-2 excursion has not been previously identified.

Each of the negative C isotope excursions demonstrates strong spatial heterogeneity among the sections studied. For the cap-carbonate-associated EN1 (or EN1-1 at ZCP), the $\delta^{13}C_{carb}$ and $\delta^{13}C_{org}$ profiles show a decoupling of the stratigraphic trends at ZCP and JLW but sympathetic trends at SDP (Fig. 2). At ZCP, $\delta^{13}C_{carb}$ has a mean of -0.4 ‰ (SD = ±1 ‰) in the 3 m of cap carbonate and reaches +5.3 ‰ at ~20 m. The $\delta^{13}C_{org}$ values generally remain less variable (-29.4 ± 0.9 ‰; mean ± SD) in EN1-1, although two basal samples have values of > -28 ‰. At JLW, $\delta^{13}C_{carb}$ values show large variability but generally increase from -4 ‰ to +5‰ in the basal 30 m. The $\delta^{13}C_{org}$ values correspondingly decrease up section from -25 ‰ to -30 ‰ in the 6 m of cap carbonate and are invariant thereafter. In contrast, at SDP, $\delta^{13}C_{carb}$ values decrease up section from -2.5 ‰ to -5.4 ‰ in the 6 m of cap carbonate and gradually increase to +5 ‰ by 40 m. The $\delta^{13}C_{org}$ values correspondingly decrease up section from -25 ‰ to -34 ‰ in the 6 m of cap carbonate and gradually increase to -25 ‰ by ~40 m.

285 The EN1-2 excursion was observed only in the ZCP section and lacks an equivalent
286 within Member II at JLW and SDP. This excursion is marked by a coupling between the $\delta^{13}C$
287 profiles for carbonate and organic carbon. Specifically, between 29 and 43 m, $\delta^{13}C_{carb}$ and
288 $\delta^{13}C_{org}$ decrease up section from +5 to –8 ‰ and from –28 to –31 ‰, respectively, and
289 between 43 and 55 m, they recover to +6 ‰ and –27 ‰, respectively (Fig. 2A).
290 The EN2 excursion is more distinct at JLW and SDP compared to ZCP (Fig. 2). At JLW,
291 $\delta^{13}C_{carb}$ decreases up section from +4 to –10 ‰ between 68 and 76 m and recovers to +4 ‰
292 by 85 m. At SDP, $\delta^{13}C_{carb}$ decreases up section from +4 to –2 ‰ between 60 and 70 m and
293 returns to +5 ‰ by 75 m. At ZCP, only two small negative shifts from +5 to +1 ‰ are present
294 between 72 and 92 m. No significant variations were observed in coexisting $\delta^{13}C_{org}$ records of
295 EN2 at the three study sites (Fig. 2).
296 The youngest negative C isotope excursion, EN3 (Fig. 2), is thought to be equivalent to
297 the SE as described in Oman (Fike et al., 2006), Australia (Swanson-Hysell et al., 2010), and
298 the western United States (Corsetti and Kaufman, 2003), with a U-Pb age of 551 ± 0.7 Ma for
299 the upper limb of the excursion in China (Condon et al., 2005). The EN3 event at JLW shows
300 three distinct intervals of $\delta^{13}C_{carb}$ variation (from base to top): (i) a negative shift from +5 to –
301 9 ‰ over ~20 m (EN3a), (ii) a stable interval of roughly –9 ‰ over ~33 m (EN3b), and (iii) a
302 recovery from –9 to –2 ‰ over > 10 m (EN3c). The $\delta^{13}C_{org}$ profile is decoupled from $\delta^{13}C_{carb}$,
303 showing (i) an up section increase from –30 to –27 ‰ in EN3a; (ii) a general decrease to –39 ‰
304 from –27 ‰ in EN3b, although with large sample-to-sample variability; and (iii) a recovery
305 to –34 ‰ from –39 ‰ in EN3c. The shallower ZCP and deeper SDP sections show different
306 $\delta^{13}C_{carb}$ features: (i) EN3a corresponds to a negative shift up section from +5 to –1 ‰ over

307 ~20 m at ZCP and from +5 to 0 ‰ over ~5 m at SDP, (ii) EN3b is not clearly expressed at
308 ZCP but is marked by values of ca. +1.5 ‰ over ~60 m at SDP, and (iii) EN3c shows a
309 recovery from –1 ‰ to +3 ‰ at ZCP and a pronounced minimum of –8.3 ‰ followed by a
310 recovery to +0.1 ‰ at SDP. The $\delta^{13}C_{org}$ profiles of the ZCP and SDP sections reveal complex
311 variation that is both coupled and decoupled relative to the respective $\delta^{13}C_{carb}$ records (Fig.
312 2).
313
314 **Evaluation of diagenetic influences on $\delta^{13}C_{carb}$**
315 Primary $\delta^{13}C_{carb}$ values can be altered by diagenesis, including recrystallization, which
316 has been suggested previously as a mechanism for local $\delta^{13}C_{carb}$ variability during the Shuram
317 (Derry, 2010a; Swart and Kennedy, 2012; Schrag et al., 2013). To avoid potential effects of
318 secondary alteration on $\delta^{13}C_{carb}$, we collected microcrystalline dolostones wherever possible
319 and removed any obvious weathered surfaces, veins, and cements prior to powdering.
320 Furthermore, diagenetic alteration of $\delta^{13}C_{carb}$ can be evaluated through multiple geochemical
321 approaches (Brand, 2004). Because strontium is expelled from marine carbonates,
322 particularly aragonite, while manganese is incorporated under the influence of reducing fluids,
323 Mn/Sr ratios can be used to evaluate the degree of alteration (Kaufman and Knoll, 1995).
324 Previous studies suggested that Mn/Sr of < 3 is consistent with little to no alteration (Derry et
325 al., 1992; Kaufman et al., 1992, 1993). However, diagenetic fluids generally contain much
326 less carbon than carbonate rocks, which favors the buffering capacity of carbonate C relative
327 to DIC derived from organic matter remineralization. Therefore, samples with Mn/Sr as high
328 as 10 are likely to preserve primary $\delta^{13}C_{carb}$ values (Kaufman and Knoll, 1995). Most of our

329 samples (79 %) have Mn/Sr <3, and nearly all of them (95 %) have Mn/Sr <10, suggesting
330 that the $\delta^{13}C_{carb}$ profiles of the study sections preserve near-primary marine carbonate signals
331 (Fig. 3). A small number of samples (five in EN1-1 and IP at ZCP, four in EN1 at JLW, and
332 four in EN1 and EN3c at SDP) have Mn/Sr > 10, suggesting possible diagenetic alteration of
333 their $\delta^{13}C$ values.

334 Because post-depositional alteration of marine carbonate rocks commonly produces a
335 decrease in both $\delta^{13}C$ and $\delta^{18}O$ values, extremely low $\delta^{18}O$ values (commonly < –10 ‰) and
336 positive co-variation between C and O isotopes have been cited as evidence for a diagenetic
337 origin of negative isotope excursions (Knauth and Kennedy, 2009), including the SE
338 (Grotzinger et al., 2011, Derry, 2010a). Samples with $\delta^{18}O$ values of < –10 ‰ are mostly
339 associated with EN1 at JLW and SDP, EN1-2 at ZCP, and the lower portion of EN3b at JLW
340 (Fig. 3). Indeed, the EN1-2 at ZCP is associated with abundant phosphorite deposition, which
341 is susceptible to diagenetic alteration of carbonates (Kaufman and Knoll, 1995). Opposite to
342 the described effects of diagenesis on $\delta^{13}C_{carb}$-$\delta^{18}O_{carb}$, however, the ZCP section shows no
343 significant $\delta^{13}C_{carb}$-$\delta^{18}O_{carb}$ covariation for any excursion (Fig. 4A), including EN3 ($r^2 = 0.0$).
344 The SDP section exhibits minor to moderate $\delta^{13}C_{carb}$-$\delta^{18}O_{carb}$ covariation for each excursion,
345 but the correlations are negative rather than positive for the EN2 and EN3 (Fig. 4C)—again,
346 the opposite of that expected from diagenesis (Knauth and Kennedy, 2009). These correlation
347 relationships thus do not support significant diagenetic alteration of $\delta^{13}C_{carb}$ values in these
348 sections. In fact, the widespread lack of systematic positive covariation between $\delta^{13}C_{carb}$ and
349 $\delta^{18}O_{carb}$ in other sections of the Yangtze Platform strongly supports a non-diagenetic origin
350 for EN3 found across the Yangtze Platform (Lu et al., 2013).

The JLW section exhibits minor to moderate $\delta^{13}C_{carb}$-$\delta^{18}O_{carb}$ positive covariation for each excursion (Fig. 4B), including EN3 ($r^2 = 0.22$). It is possible that these positive covariation patterns reflect some degree of diagenetic overprinting of original $\delta^{13}C_{carb}$ values during dolomitization and early burial more generally as suggested by some samples with elevated Mn/Sr and low $\delta^{18}O_{carb}$ values (Fig. 3B). However, a few lines of evidence suggest that diagenetic alteration for the EN3 of JLW is insignificant. First, the stratigraphic consistency of EN3 at JLW to other age-equivalent $\delta^{13}C_{carb}$ profiles across the Yangtze Platform (Lu et al., 2013) and its global correlations to other Ediacaran $\delta^{13}C_{carb}$ profiles in India (Kaufman et al., 2006), Oman (Fike et al., 2006; Osburn et al., 2015), Australia (Calver, 2000; Swanson-Hysell et al., 2010), the southwestern USA (Corsetti and Kaufman, 2003), and northern Mexico (Loyd et al., 2013) suggest that primary secular patterns have been preserved—although local overprints on the global signal are to be expected (as discussed below). Second, petrographic observations reveal that most carbonates from the EN3 in the JLW section are fine grained and uniformly microcrystalline (Lu et al., 2013; McFadden et al., 2008)—inconsistent with a diagenetic origin. Third, the EN3 excursion at JLW is characterized by smooth $\delta^{13}C$ variation that is independent of lithofacies changes (dolostone-limestone-black shales) (Lu et al., 2013), which is also consistent with a primary origin of the EN3 signal. Fourth, compared with calcite precipitation, dolomite formation can result in significantly greater oxygen isotope fractionation (up to 5 ‰) (e.g., Vasconcelos et al., 2005). We note that largely invariant $\delta^{18}O$ values are found throughout EN3 in exclusively dolomitic successions (ZCP and SDP sections), but a significant decrease in $\delta^{18}O$ values is found in the JLW section within the transition from dolomite beds (< 120 m) to

overlying limestone beds (120-140 m) without a corresponding change in $\delta^{13}C_{carb}$ (Fig. 4D, and Table S1). This relationship is consistent with mineralogical control of carbonate $\delta^{18}O$ and a non-diagenetic origin of $\delta^{13}C_{carb}$ variation in the EN3 interval of the sections studied. Similar patterns of $\delta^{18}O$-$\delta^{13}C_{carb}$ for the transition from dolomite to limestone are observed in other sections from the Yangtze Platform (Lu et al., 2013), suggesting that the EN3 signal basin wide is of primary origin.

Recent studies provide additional evidence that the SE trends recorded in sections on other continents also represent a primary seawater signal. For example, in Australia, Mg- and Ca-isotope data—along with [Mg], [Mn], and [Sr] data from carbonates of the Ediacaran-aged Wonoka Formation—indicate that the most pristine samples carry strongly negative $\delta^{13}C_{carb}$ signals (–7 to –8 ‰) (Husson et al., 2015), consistent with a primary origin. Furthermore, the carbon isotope compositions of extractable long-chain (> C20) *n*-alkanes and mid-chain monomethyl alkanes from the SE strata in Oman were found to be as low as –40 ‰ (Lee et al., 2015), which is rare for marine rocks of any age and provides evidence for a major carbon cycle perturbation in conjunction with the SE in Oman. Additionally, our CAS concentration data from the Doushantuo and those previously published from global distributed sections—Oman, Mexico, and Death Valley—provide evidence against meteoric diagenesis being responsible for the SE (Fig. 6). Specifically, work evaluating CAS concentrations during aragonite-to-calcite neomorphism of Pleistocene coral heads in the presence of meteoric fluids found that CAS concentrations decrease dramatically (Gill et al., 2008), often by orders of magnitude, because sulfate concentrations in meteoric fluids are significantly lower than those of seawater. This relationship allows for rock-buffered $\delta^{34}S_{CAS}$

during meteoric alterations but with large decreases in CAS concentration (Gill et al., 2008). Opposite to this, the CAS concentrations in the Doushantuo Formation of South China, the Khufai and Shuram formations of Oman (Fike et al., 2006; Osburn et al., 2015), the Johnnie Formation of Death Valley (Kaufman et al., 2007), and the Clemente Formation of Mexico (Loyd et al., 2012) all increase during the SE (Fig. 6).

Taken together, our integrated geochemical, mineralogical, petrographic, and stratigraphic evidence from this study and previous investigations (Lu et al., 2013; Tahata et al., 2013; Husson et al., 2015; Lee et al., 2015; Osburn et al., 2015) indicates that the EN2 and EN3 (SE) on the Yangtze Platform represent primary seawater signals and that the EN3 is most likely a global signal. Given the possibility of significant post-depositional alteration for the EN1 of our sections (EN1-1 and EN1-2 at ZCP) and the significance of the SE, we limit our discussion below mainly to EN3.

Elevated continental weathering and coastal marine sulfate concentration during the SE

To provide a context for interpreting the mechanisms driving the observed spatial heterogeneity in the SE, we evaluated proxies for weathering rates (Sr isotopes) and marine sulfate availability (CAS concentrations and isotope composition). First, we examined $^{87}Sr/^{86}Sr$ ratio—a proxy for continental weathering (Richter et al., 1992). In South China, the Doushantuo negative C isotope excursions were accompanied by elevated $^{87}Sr/^{86}Sr$ ratios, with the highest $^{87}Sr/^{86}Sr$ ratios during the SE (up to 0.708958; Fig. 5). Relatively elevated $^{87}Sr/^{86}Sr$ ratios provide evidence for enhanced continental weathering during these isotopic events (Sawaki et al., 2008, 2010; Cui et al., 2015). A compilation of data from various

continents shows that the SE was globally tied to the highest $^{87}Sr/^{86}Sr$ ratios for the Ediacaran (Fig. 5), consistent with the strongest continental weathering during the SE. An increase in weathering rate might be related to an increase in global tectonic activity associated with global microcontinent collisions that stitched Gondwana during the middle Ediacaran (see reviews in Halverson et al., 2010, and Och and Shields-Zhou, 2012); however, details of the mechanisms behind possible increases in weathering rates remain uncertain.

Second, we compared paired CAS concentration and $\delta^{34}S_{CAS}$ data with $\delta^{13}C_{carb}$ results from the JLW section, which is characterized by the most prominent negative $\delta^{13}C_{carb}$ excursion during the SE among the sections we studied. Furthermore, we compiled the paired C-S data available from other SE successions in Mexico (Loyd et al., 2012), southwest USA (Kaufman et al., 2007), and Oman (Fike et al., 2006; Osburn et al., 2015) (Fig. 6). The results from JLW demonstrate that the SE was accompanied by a parallel negative shift in $\delta^{34}S_{CAS}$ (up section from > +40 ‰ to < +10 ‰), as well as elevated CAS concentration (from < 100 ppm to > 1000 ppm) (Fig. 6A). These coupled trends suggest that marine sulfate concentrations were elevated during the SE relative to before. Importantly, generally similar coupling between the C-S data are observed for all the compiled successions (Fig. 6B-D), despite their global distribution, suggesting that the elevated marine sulfate concentration and depleted isotopic composition during the SE were a global phenomenon. Indeed, an increase in seawater sulfate concentration has been inferred for the SE at all previously investigated localities (Fike et al., 2006; McFadden et al., 2008; Li et al., 2010; Kaufman et al., 2007; Loyd et al., 2013; Osburn et al., 2015). The increase in CAS concentration and negative excursion in $\delta^{34}S_{CAS}$ in association with the SE have been previously interpreted to reflect an

increase in the global marine sulfate reservoir in response to atmospheric and marine oxygenation during this period (Fike et al., 2006; Loyd et al., 2013; Kaufman et al., 2007; Osburn et al., 2015).

Interestingly, however, different patterns for this C-S coupling are observed among the different continental sites. For example, the magnitudes of the negative shift in $\delta^{34}S_{CAS}$ and increasing CAS concentration in Oman are generally < 15 ‰ and up to > 10,000 ppm (Fig. 6D), respectively, which are substantially different from those observed in South China and other places (Fig. 6A-C). Furthermore, detailed analyses indicate that the negative shift of $\delta^{34}S_{CAS}$ and the elevation of CAS concentration in Oman are associated mainly with shallow waters (Huqf area) rather than deep waters (Moutain area) (Osburn et al., 2015; Fig. 6D). These observations together indicate that the general increase in marine sulfate concentration during the SE was a global phenomenon specific to shallow waters and that local heterogeneities in the magnitude and distribution occurred.

Interpreting the spatial heterogeneity of the Shuram Excursion

Previous interpretations of the Shuram $\delta^{13}C_{carb}$ excursion have linked the increase in marine sulfate concentrations to oxidation of a formerly anoxic deep ocean with a large pool of DOC (e.g., Fike et al., 2006). However, recent redox proxy studies have provided evidence against pervasive ventilation of the deep ocean during the SE (e.g., Li et al., 2010; Dahl et al., 2010; Johnston et al., 2013; Sperling et al., 2015; Sahoo et al., 2016). Furthermore, oxidant mass balance models for ocean ventilation and DOC oxidation driving the excursion highlight that such a scenario is unlikely, as both marine oxygen and sulfate would be

461 inadequate (Bristow and Kennedy, 2008). Together, these modelling and redox proxy studies
462 suggest that if the SE records an oxidation event, it must have been limited in its areal extent.

463 Our $\delta^{13}C_{carb}$ dataset provides additional new constraints in this regard. A distinct feature
464 of our proximal-to-distal transect from the Doushanto Formation is that the magnitude,
465 timing, and $\delta^{13}C_{carb}$-$\delta^{13}C_{org}$ relationship of the negative $\delta^{13}C_{carb}$ excursions differ among the
466 sites. The high spatial heterogeneity of these primary excursions suggests that the $\delta^{13}C_{carb}$
467 data for the SE at least partially reflect local controls on DIC in shelf settings. Our claim of
468 local heterogeneity in the $\delta^{13}C_{DIC}$ during the SE is supported by examples from outside of the
469 Doushantuo Formation. For example, the $\delta^{13}C_{carb}$ record for Shuram-aged carbonates from
470 northwest Canada ranges from -2 to -8.5 ‰, similarly pointing to local controls (MacDonald
471 et al., 2013), and the most pristine carbonates from the SE captured in the Wonoka Formation
472 have $\delta^{13}C_{carb}$ of -7 to -8 ‰ (Husson et al., 2015). Additional constraints from the $\delta^{13}C$ of
473 compound-specific biomarkers in Oman suggest that the primary excursion of the SE may
474 have actually been as small 5-7 ‰ at that locality (Lee et al., 2015). Together, this evidence
475 implies that the global shift in $\delta^{13}C_{DIC}$ during the SE may not have been as extreme as the
476 -17 ‰ of $\delta^{13}C$ excursion observed in the carbonate record at some localities and that models
477 should consider local processes driving heterogeneity in the local $\delta^{13}C_{DIC}$.

478 Here, in light of the observations of spatial heterogeneity in $\delta^{13}C$ and inferred oxidation,
479 we propose an updated conceptual model for the mechanism behind the negative $\delta^{13}C_{carb}$ of
480 the SE (Fig. 7). As shown by previous work, the Ediacaran oceans were redox stratified with
481 anoxic deep waters (Canfield et al., 2008; Li et al., 2010, 2015; Sahoo et al., 2016) and low in
482 sulfate (< 2 mM; Loyd et al., 2012; Osburn et al., 2015). Within this framework, we propose

483 that the strong continental weathering during the SE, as suggested by the highest $^{87}Sr/^{86}Sr$
484 ratios (see Fig. 5 and previous section), may have greatly elevated continental nutrient fluxes
485 into coastal oceans, resulting in unusually high coastal productivity. Recent biogeochemical
486 modelling shows that at low atmospheric pO_2 levels (e.g., < 2.5% present atmospheric level
487 or PAL), the distribution of O_2 in the surface ocean is controlled principally by marine
488 productivity (i.e., O_2 release), with the highest dissolved O_2 levels restricted primarily to
489 areas of high productivity (Reinhard et al., 2016). Thus, any elevation of coastal productivity
490 might have resulted in coastal surface-ocean oxygenation if the atmospheric pO_2 levels prior
491 to and during the SE were low enough. Indeed, recent reviews noted that Ediacaran pO_2
492 levels might have been only a few per cent of PAL, although a large range has been suggested
493 (see reviews by Lyons et al., 2014, and Sperling et al., 2015). Coastal surface ocean
494 oxygenation could in theory have resulted in less oceanic pyrite burial and in turn more
495 negative $\delta^{34}S_{CAS}$ and higher sulfate concentration in the local surface waters (i.e., higher
496 [CAS]). Another possibility is that increased continental weathering may have elevated the
497 riverine sulfate flux into coastal oceans. Ultimately, increased marine oxidant availability led
498 to oxidation in formerly anoxic, relatively shallow settings while maintaining redox
499 stratification (i.e., persistently anoxic deep waters) across the event—resulting in both
500 vertical and lateral gradients in oxidant distribution.

501 Given an increase in shallow marine oxidant availability (O_2 and sulfate), we assume that
502 the source of the isotopically light $\delta^{13}C_{DIC}$ was more widespread oxidation (likely with higher
503 rates and greater depth penetration of those oxidants) in shallow waters adjacent to
504 persistently anoxic subsurface waters containing high concentrations of reduced carbon. We

note that elevated reduced carbon concentrations in the Ediacaran ocean have been assumed in previous work, but have yet to be proven, and that this study provides no additional constraints on the possible source of that carbon. Previous studies favored DOC (Rothman et al., 2003; Fike et al., 2006; McFadden et al., 2008; Wang et al., 2015; 2016) or other forms of organic carbon such as fresh or aged organic matter (Lee et al., 2015). Within this framework, the $\delta^{13}C$ of local carbonate sediments was determined by mixing of global marine background DIC (DIC_{bg}) and isotopically light DIC derived from oxidation of reduced carbon (DIC_{rc}) on a large scale—along with DIC_{rc} generated locally through intense oxidation coupled to heterogeneous supplies of O_2 and perhaps sulfate (see lower-left insert in Fig. 7). As such, both spatial variations in $\delta^{13}C_{DIC}$ and the extremely negative $\delta^{13}C_{carb}$ values observed through the SE are mostly a product of local variation in rates of reduced-carbon oxidation in shelf settings rather than shifts in global seawater $\delta^{13}C_{DIC}$. Thus, our proposed local, mostly shelf oxidation of subsurface reduced carbon—as opposed to a large shift in global marine $\delta^{13}C_{DIC}$ and comprehensive ocean ventilation—minimizes the likelihood of the inadequate oxidant supplies imagined in previous studies, which assumed whole-ocean oxygenation and corresponding shifts in $\delta^{13}C$ on the same scale (Bristow and Kennedy, 2008).

Our model can account for the general patterns of spatial heterogeneity of the SE (i.e., EN3) observed in this study. Specifically, relatively low initial reduced carbon availability in nearshore areas (represented here by ZCP) and low oxidant availability to distal areas (represented here by SDP) would have resulted in maximum local DIC production in mid-shelf areas (represented here by JLW) during the EN3a-EN3b (Fig. 7). This region would

have marked the interface between deeper anoxic waters rich in reduced carbon and shallow regions relatively richer in O_2 and with proximal riverine sulfate inputs that rose due to enhanced, tectonically induced weathering. The influence of local DIC_{rc} production is seen in the $\delta^{13}C_{carb}$ profiles of mid-shelf sections, including JLW (this study) and nearby sections (e.g., Tianjiayuanzi; Lu et al., 2013), which exhibit exceptionally large EN3 excursions (Fig. 2B). In contrast, nearshore sections, including ZCP (this study) and nearby Hushan-Dayukou (Zhu et al., 2013) as well as those sections, such as Zhongling (Li et al., 2010), that were located on shallow shelf margin rims with low reduced carbon availability (Fig. 7), exhibit significantly smaller EN3 excursions (Fig. 2A). During the late-stage of the SE, reduced local DIC_{rc} availability via persistent consumption of reduced carbon at the nearshore ZCP and mid-shelf JLW locales are consistent with the observed recovery of $\delta^{13}C_{carb}$ to more positive values in EN3c (Fig. 2A-B).

Our conceptual model still requires recognition of additional details of the SE heterogeneity (e.g., the large negative $\delta^{13}C_{carb}$ excursion observed in EN3c at the distal SDP in this study), analogous heterogeneous $\delta^{13}C_{carb}$ at other, globally distributed SE settings, as well as proxy evidence for increased nutrient availability and the source of the isotopically light DIC. However, in principle, our heterogeneous oxidation model can be used to explain existing $\delta^{13}C_{carb}$ records of the SE from the Yangtze Platform as well as those seen in other regions simply by changing the mixing ratio of locally produced DIC and the open seawater. Our model defines a general spatial framework based on the availability of oxidants and reduced carbon in the ocean, which predicts that the SE was recorded most prominently in shelf settings where both oxidants and reduced carbon were in ample supply (e.g., the JLW

549 section of this study). Indeed, the most prominent expressions of the SE worldwide are found
550 in shallow-marine carbonate successions (reviewed by Grotzinger et al., 2011). In South
551 China, the SE is particularly well-developed in mid-shelf to upper-slope settings and in
552 intra-shelf basins (Lu et al., 2013; Tahata et al., 2013; Wang et al., 2016), which reflects the
553 optimal balance of local surface-ocean oxidant availability and anoxic, subsurface
554 distributions of reduced carbon.
555
556 **Interpreting the $\delta^{13}C_{org}$ records of the SE in terms of elevated continental weathering**
557 The global record of the SE, including the EN3 in South China, is also notable for the
558 lack of coupling of $\delta^{13}C_{carb}$ and $\delta^{13}C_{org}$ (Fig. 2) (Grotzinger et al., 2011; Lee et al., 2013). This
559 feature has been explained by varying inputs of detrital, relatively ^{13}C-enriched organic
560 matter (OM_{det}) and ^{13}C-depleted marine OM (OM_{mar}) (i.e., OM in sediment = OM_{det} + OM_{mar};
561 see details in Johnston et al., 2012, and Jiang et al., 2012). The OM_{det} may have been
562 relatively ^{13}C-enriched, even if originally marine, because it experienced significant thermal
563 maturation during burial prior to uplift and reworking. Thermal processing would have
564 preferentially expelled isotopically light hydrocarbons, thus increasing the $\delta^{13}C$ of the
565 remaining organic matter (Des Marais et al., 1992). High rates of continental weathering are
566 suggested by our compiled Sr isotope records (Fig. 5). Greatly enhanced continental
567 weathering may have generated large nutrient fluxes while simultaneously stimulating
568 delivery of significant amounts of OM_{det} into the coastal oceans. The collective result of these
569 processes would have been an increase in $\delta^{13}C_{org}$ as observed during the early to middle stage
570 of the SE at all of our locations (EN3a and lower portion of EN3b in Fig. 2). Hand in hand

571 with the decline of continental weathering as suggested by decreasing $^{87}Sr/^{86}Sr$ ratios (Fig. 5)
572 and anticipated decrease of OM_{det} input during the later stage of the SE, the relative
573 contribution of OM_{det} versus OM_{mar} to sedimentary organic matter gradually decreased. As a
574 result, a decrease in $\delta^{13}C_{org}$ occurred, as observed in the upper portion of the EN3b and the
575 entire EN3c at all of our study sites (Fig. 2). Minimum $\delta^{13}C_{org}$ values of < –38 ‰ ultimately
576 developed in the more distal JLW and SDP sections, suggesting significant contributions of
577 chemotrophic and/or methanotrophic biomass to OM_{mar} under anoxic bottom waters (Jiang et
578 al., 2012; Wang et al., 2016). Therefore, the $\delta^{13}C_{org}$ records of the SE also support our model
579 in which greatly elevated weathering of the continents served as a trigger for these negative
580 $\delta^{13}C_{carb}$ excursions.
581
582 **CONCLUSIONS**
583
584 Integrated $\delta^{13}C_{carb}$-$\delta^{13}C_{org}$ data from the inner-shelf section of Zhangcunping and the
585 intra-shelf-basin and upper-slope sections of Jiulongwan and Siduping, respectively, reveal
586 large spatial heterogeneity in Ediacaran carbon isotope records, particular for the globally
587 distributed Shuram Excursion (SE). Combined geochemical, mineralogical, petrographic, and
588 stratigraphic data indicate a primary marine signature for at least the SE in South China.
589 Globally elevated $^{87}Sr/^{86}Sr$ ratios during the SE suggest that the SE was tied to elevated
590 continental weathering during the mid-Ediacaran. Paired concentration and $\delta^{34}S$ data for
591 carbonate-associated sulfate from South China, Mexico, southwest USA, and Oman indicate
592 an increase in marine sulfate during the SE, but with different magnitudes and patterns among

593 the globally distributed sites. In light of these observations, we propose a heterogeneous
594 oxidation model involving greater oxygenation of the surface ocean in coastal regions to
595 explain the SE and the high spatial heterogeneity among the observed records for $\delta^{13}C_{carb}$ and
596 coexisting $\delta^{13}C_{org}$. Specifically, we argue that elevated continental weathering brought high
597 nutrient fluxes into coastal oceans, which resulted in elevation of coastal primary productivity,
598 greater surface-ocean oxygenation as a consequence, and local elevation of marine sulfate
599 concentration. The latter would reflect the combined effects of greater riverine sulfate inputs
600 and reduced pyrite burial beneath the more widely oxic surface waters along the continental
601 margins. Thus, the spatial $\delta^{13}C_{carb}$ patterns of the SE were controlled primarily by spatially
602 varying extents of oxidation of reduced carbon by oxidants (mainly O_2 and sulfate) in surface
603 waters mostly in shelf areas. The reduced carbon was plentiful in the persistently
604 oxygen-deficient deeper waters of the stratified water column and could be supplied to the
605 shallower waters. The elevated local oxidation of subsurface reduced carbon mainly in shelf
606 settings proposed in our model minimizes the likelihood of the inadequate supply of oxidant
607 suggested in previous research of the SE, which assumed whole-ocean oxygenation.
608 Independent of the mechanistic specifics presented here, however, the evidence for spatial
609 heterogeneity in $\delta^{13}C$ presented in this study must be accounted for in future models of the
610 SE.
611

612 ## ACKNOWLEDGMENTS

613

We thank G. Love, M. Zhu, X. Chu, M. Osburn, L. Feng, Z. Zhang, C. Jin, B. Chang, H. Song and L. Tian for their field and laboratory assistance, data collection and helpful discussions. We thank the National Key Basic Research Program of China (Grant 2013CB955704) and the State Key R&D project of China (Grant 2016YFA060104) as well as the NSF-ELT program and the NASA Astrobiology Institute (TWL) for funding.

AUTHOR CONTRIBUTIONS

C.L. designed this research with input from T.W.L., G.L., J.H., S.X., N.J., and T.J.A. C.L., G.L., J.H., M.C., W.S., Z.A., and J.T. collected samples in field, and G.L., J.H., W.S., and Z.A. performed laboratory analyses. C.L., D.S.H., W.S., M.C. and T.W.L. analysed the data. C.L., D.S.H., T.J.A., and T.W.L. wrote this article with significant input from all co-authors.

REFERENCES

An Z, Jiang G, Tong J, Tian L, Ye Q, Song H, Song H (2015) Stratigraphic position of the Ediacaran Miaohe biota and its constrains on the age of the upper Doushantuo $\delta^{13}C$ anomaly in the Yangtze Gorges area, South China. *Precambrian Research* **271**, 243–253.

Brand, U (2004) Carbon, oxygen and strontium isotopes in Paleozoic carbonate components: an evaluation of original seawater-chemistry proxies. *Chemical Geology*, *204*(1), pp. 23-44.

Bristow T, Kennedy MJ (2008) Carbon isotope excursions and the oxidant budget of the Ediacaran atmosphere and ocean. *Geology* **36**, 863–866.

636 Burns SJ, Matter A (1993) Carbon isotopic record of the latest Proterozoic from Oman. *Eclogae*
637 *Geologicae Helvetiae* **86 (2)**, 595–607.
638 Calver CR (2000) Isotope stratigraphy of the Ediacarian (Neoproterozoic III) of the Adelaide Rift Complex,
639 Australia, and the overprint of water column stratification. *Precambrian Research* **100,** 121–150.
640 Canfield DE, Poulton SW, Knoll AH, Narbonne GM, Ross G, Goldberg T, Strauss H (2008) Ferruginous
641 conditions dominated later Neoproterozoic deep-water chemistry. *Science*, **321**, 949–952.
642 Condon D, Zhu M, Bowring S, Wang W, Yang J (2005) U-Pb ages from the Neoproterozoic Doushantuo
643 Formation, China. *Science* **308,** 95–98.
644 Corsetti FA, Kaufman AJ (2003) Stratigraphic investigations of carbon isotope anomalies and
645 Neoproterozoic ice ages in Death Valley, California. *Geological Society of America Bulletin* **115,** 916–
646 932.
647 Cui H, Kaufman AJ, Xiao S, Zhu M, Zhou C, Liu X-M (2015) Redox architecture of an Ediacaran ocean
648 margin: Integrated chemostratigraphic ($\delta^{13}C$–$\delta^{34}S$–$^{87}Sr/^{86}Sr$–Ce/Ce*) correlation of the Doushantuo
649 Formation, South China. *Chemical Geology* **405**, 48–62.
650 Dahl TW, Hammarlund EU, Anbar AD, Bond DPG, Gill BC, Gordon GW, Knoll AH, Nielsen AT,
651 Schovsbo NH, Canfield DE (2010) Devonian rise in atmospheric oxygen correlated to the radiations
652 of terrestrial plants and large predatory fish. *Proceedings of the National Academy of Sciences of the*
653 *United States of America* **107**, 17911–17915.
654 Derry LA (2010a) A burial diagenesis origin for the Ediacaran Shuram–Wonoka carbon isotope anomaly.
655 *Earth and Planetary Science Letters* **294**, 152–162.
656 Derry LA (2010b) On the significance of $\delta^{13}C$ correlations in ancient sediments. *Earth and Planetary*
657 *Science Letters* **296**, 497–501.

658 Derry LA, Kaufman AJ, Jacobsen SB (1992) Sedimentary cycling and environmental change in the Late
659 Proterozoic: evidence from stable and radiogenic isotopes. *Geochimica et Cosmochimica Acta*
660 **56**:1317–1329.
661 Des Marais DJ, Strauss H, Summons RE, Hayes JM (1992) Carbon isotope evidence for the stepwise
662 oxidation of the Proterozoic environment. *Nature* **359**: 605–609.
663 Droser ML, Gehling JG (2015) The advent of animals: the view from the Ediacaran. *Proceedings of the*
664 *National Academy of Sciences of the United States of America* **112**, 4865–4870.
665 Fike DA, Grotzinger JP, Pratt LM, Summons RE (2006) Oxidation of the Ediacaran Ocean. *Nature* **444,**
666 744–747.
667 Foden J, Barovich KM, O'Halloran M (2001) Sr-isotopic evidence for Late Neoproterozoic rifting in the
668 Adelaide geosyncline at 586 Ma: implications for a Cu ore forming fluid flux. *Precambrian Research*
669 **106**, 291–308.
670 Grotzinger JP, Fike DA, Fischer WW (2011) Enigmatic origin of the largest-known carbon isotope
671 excursion in Earth's history. *Nature Geoscience* **4,** 285–292.
672 Gill BC, Lyons TW, Frank TD (2008) Behavior of carbonate-associated sulfate during meteoric diagenesis
673 and implications for the sulfur isotope paleoproxy. *Geochimica et Cosmochimica Acta* **72**, 4699–4711.
674 Halverson GP, Hurtgen MT, Porter SM, Collins AC (2010) Neoproterozoic – Cambrian biogeochemical
675 evolution. In: Gaucher C, Sial AN, Halverson GP, Frimmel H (Eds.), Neoproterozoic – Cambrian
676 Tectonics, Global Change and Evolution: A Focus on Southwestern Gondwana, Dev. Precambrian
677 Geol., vol. 16. Elsevier, pp. 351–365.
678 Husson JM, Higgins JA., Maloof AC, Schoene B (2015) Ca and Mg isotope constraints on the origin of
679 Earth's deepest δ13C excursion. *Geochimica et Cosmochimica Acta* **160**, 243–266.

680 Jiang G, Kaufman AJ, Christie-Blick N, Zhang S., Wu H (2007) Carbon isotope variability across the
681 Ediacaran Yangtze platform in South China: implications for a large surface-to-deep ocean $\delta^{13}C$
682 gradient. *Earth and Planetary Science Letters* **261,** 303–320.
683 Jiang G, Wang X, Shi X, Zhang S, Xiao SH, Dong J (2010) Organic carbon isotope constraints on the
684 dissolved organic carbon (DOC) reservoir at the Cryogenian-Ediacaran transition. *Earth and Planetary*
685 *Science Letters* **299,** 159–168.
686 Jiang G, Wang X, Shi X, Xiao S, Zhang S, Dong J (2012) The origin of decoupled carbonate and organic
687 carbon isotope signatures in the early Cambrian (ca.542–520 Ma) Yangtze platform. *Earth and*
688 *Planetary Science Letters* **317–318**, 96–110.
689 Jiang G, Shi X, Zhang S, Wang Y, Xiao S (2011) Stratigraphy and paleogeography of the Ediacaran
690 Doushantuo Formation (ca. 635–551 Ma) in South China. *Gondwana Research* **19**, 831–849.
691 Johnston DT, Macdonald FA, Gill BC, Hoffman PF, Schrag DP (2012) Uncovering the Neoproterozoic
692 carbon cycle. *Nature* **483,** 320–323.
693 Johnston DT, Poulton SW, Tosca NJ, O'brien T, Halverson GP, Schrag DP, Macdonald FA (2013)
694 Searching for an oxygenation event in the fossiliferous Ediacaran of northwestern Canada. *Chemical*
695 *Geology* **362,** 273–286.
696 Kaufman AJ, Corsetti FA, Varni MA (2007) The effect of rising atmospheric oxygen on carbon and sulfur
697 isotope anomalies in the Neoproterozoic Johnnie Formation, Death Valley, USA. *Chemical Geology*
698 **237**, 47–63.
699 Kaufman AJ, Jacobsen SB, Knoll AH (1993) The Vendian record of Sr- and C-isotopic variations in
700 seawater: implications for tectonics and paleoclimate. *Earth and Planetary Science Letters* **120**, 409–
701 430.

Kaufman AJ, Jiang G, Christie-Blick N, Banerjee DM, Rai V (2006) Stable isotope record of the terminal Neoproterozoic Krol platform in the Lesser Himalayas of northern India. *Precambrian Research* **147**, 156–185.

Kaufman AJ, Knoll AH, Awramik SM (1992) Biostratigraphic and chemostratigraphic correlation of Neoproterozoic sedimentary successions: Upper Tindir Group, northwestern Canada, as a test case. *Geology* **20**,181–185.

Kaufman AJ, Knoll AH (1995) Neoproterozoic variations in the C-isotopic composition of seawater: stratigraphic and biogeochemical implications. *Precambrian Research* **73**, 27–49.

Knauth LP, Kennedy MJ (2009) The late Precambrian greening of the Earth. *Nature* **460,** 728–732.

Lee C, Fike DA, Love GD, Sessions AL, Grotzinger JP, Summons RE, Fischer WW (2013) Carbon isotopes and lipid biomarkers from organic-rich facies of the Shuram Formation, Sultanate of Oman. *Geobiology* **11**, 406-419.

Lee C, Love GD, Fischer WW, Grotzinger JP, Halverson GP (2015) Marine organic matter cycling during the Ediacaran Shuram excursion. *Geology* **43**, 1103-1106.

Li C, Love GD, Lyons TW, Fike DA, Sessions AL, Chu X (2010) A stratified redox model for the Ediacaran ocean. *Science* **328**, 80–83.

Li C, Cheng M, Algeo TJ, Xie S (2015) A theoretical prediction of chemical zonation in early oceans (>520 Ma). *Science China: Earth Sciences* **58**, 1901–1909.

Liu P, Yin C, Gao L, Tang F, Chen S (2009) New material of microfossils from the Ediacaran Doushantuo Formation in the Zhangcunping area, Yichang, Hubei Province and its zircon SHRIMP U-Pb age. *Chinese Science Bulletin* **54**, 1058–1064.

723 Loyd SJ, Marenco PJ, Hagadorn JW, Lyons TW, Kaufman AJ, Sour-Tovar F, Corsetti FA (2013) Local $\delta^{34}S$
724 variability in ~580 Ma carbonates of northwestern Mexico and the Neoproterozoic marine sulfate
725 reservoir. *Precambrian Research* **224,** 551–569.
726 Loyd SJ, Marenco PJ, Hagadorn JW, Lyons TW, Kaufman AJ, Sour-Tovar F, Corsetti FA (2012) Sustained
727 low marine sulfate concentrations from the Neoproterozoic to the Cambrian: Insights from carbonates
728 of northwestern Mexico and eastern California. *Earth and Planetary Science Letters* **339-340**, 79–94.
729 Lu M, Zhu M, Zhang J, Shields-Zhou G, Li G, Zhao F, Zhao X, Zhao M (2013) The DOUNCE event at the
730 top of the Ediacaran Doushantuo Formation of South China: wide stratigraphic occurrence and
731 non-diagenetic origin. *Precambrian Research* **225**, 86–109.
732 Lyons TW, Reinhard CT, Planavsky NJ (2014) The rise of oxygen in Earth/'s early ocean and atmosphere.
733 *Nature* **506**, 307–315.
734 Macdonald FA, Strauss JV, Sperling EA, Halverson GP, Narbonne GM, Johnston DT, Kunzmann M,
735 Schrag DP, Higgins JA (2013) The stratigraphic relationship between the Shuram carbon isotope
736 excursion, the oxygenation of Neoproterozoic oceans, and the first appearance of the Ediacara biota and
737 bilaterian trace fossils in northwestern Canada. *Chemical Geology* **362**, 250–272.
738 McFadden KA, Huang J, Chu XL, Jiang GQ, Kaufman AJ, Zhou CM, Yuan XL, Xiao SH (2008) Pulsed
739 oxidation and bioloical evolution in the Ediacaran Doushantuo Formation. *Proceedings of the National*
740 *Academy of Sciences of the United States of America* **105,** 3197–3202.
741 Narbonne GM, Kaufman AJ, Knoll AH (1994) Integrated chemostratigraphy and biostratigraphy of the
742 Windermere Supergroup, northwestern Canada: implications for Neoproterozoic correlations and the
743 early evolution of animals. *Geological Society of America Bulletin* **106**, 1281–1291.

744 Och LM, Shields-Zhou GA (2012) The Neoproterozoic oxygenation event: Environmental perturbations
745 and biogeochemical cycling. *Earth-Science Reviews* **110**, 26–57.
746 Osburn MR, Owens J, Bergmann KD, Lyons TW, Grotzinger JP (2015) Dynamic changes in sulfate sulfur
747 isotopes preceding the Ediacaran Shuram Excursion. *Geochimica et Cosmochimica Acta* **170**, 204–
748 224.
749 Osburn MR, Grotzinger JP, Bergmann KD (2014) Facies, stratigraphy, and evolution of a middle Ediacaran
750 carbonate ramp: Khufai Formation, Sultanate of Oman. *American Association of Petroleum Geologists*
751 *Bulletin* **98**, 1631–1667.
752 Pecoits E, Konhauser KO, Aubet N, Heaman LM, Veroslavsky G, Stern R, Gingras MK (2012) Bilaterian
753 burrows and grazing behavior at >585 million years ago. *Science* **336**, 1693–1696.
754 Pokrovskii BG, Melezhik VA, Bujakaite MI (2006) Carbon, oxygen, strontium, and sulfur isotopic
755 compositions in Late Precambrian rocks of the Patom Complex, central Siberia: communication 1.
756 Results, isotope stratigraphy, and dating problems. *Lithology and Mineral Resources* **41 (5)**, 450–474.
757 Reinhard CT, Planavsky NJ, Olson SL, Lyons TW, Erwin DH (2016) Earth's oxygen cycle and the
758 evolution of animal life. *Proceedings of the National Academy of Sciences of the United States of*
759 *America* **113**, 8933–8938.
760 Richter FM, Rowley DB, Depaolo DJ (1992) Sr isotope evolution of seawater: the role of tectonics. *Earth*
761 *and Planetary Science Letters* **109**, 11–23.
762 Rothman DH, Hayes JM, Summons RE (2003) Dynamics of the Neoproterozoic carbon cycle. *Proceedings*
763 *of the National Academy of Sciences of the United States of America* **100**, 8124–8129.
764 Sahoo SK, Planavsky NJ, Jiang G, Kendall B, Owens JD, Wang X, Shi X, Anbar AD, Lyons TW (2016)
765 Oceanic oxygenation events in the anoxic Ediacaran ocean. *Geobiology* **14**, 457–468.

766 Sawaki Y, Ohno T, Tahata M, Komiya T, Hirata T, Maruyama S, Windley BF, Han J, Shu DG, Li Y (2010)
767 The Ediacaran radiogenic Sr isotope excursion in the Doushantuo Formation in the Three Gorges area,
768 South China. *Precambrian Research* **176**, 46–64.
769 Sawaki Y, Ohno T, Fukushi Y, Komiya T, Ishikawa T, Hirata T, Maruyama S (2008) Sr isotope excursion
770 across the Precambrian–Cambrian boundary in the Three Gorges area, South China. *Gondwana*
771 *Research* **14**, 134–147.
772 Schrag DP, Higgins JA, Macdonald FA, Johnston DT (2013) Authigenic carbonate and the history of the
773 global carbon cycle. *Science* **339,** 540–543.
774 Sperling EA, Wolock CJ, Morgan AS, Gill BC, Kunzmann M, Halverson GP, Macdonald FA, Knoll AH,
775 Johnston DT (2015) Statistical analysis of iron geochemical data suggests limited late Proterozoic
776 oxygenation. *Nature* **523**, 451–454.
777 Swanson-Hysell N, Rose CV, Calmet CC, Halverson GP, Hurtgen MT, Maloof AC (2010) Cryogenian
778 glaciation and the onset of carbon isotope decoupling. *Science* **328,** 608–611.
779 Swart PK, Kennedy MJ (2012) Does the global stratigraphic reproducibility of $\delta^{13}C$ in Neoproterozoic
780 carbonates require a marine origin? A Pliocene–Pleistocene comparison. *Geology* **40**, 87–90.
781 Tahata M, Ueno Y, Ishikawa T, Sawaki Y, Murakami K, Han J, Shu D, Li Y, Guo J, Yoshida N, Komiya T
782 (2013) Carbon and oxygen isotope chemostratigraphies of the Yangtze platform, South China:
783 decoding temperature and environmental changes through the Ediacaran. *Gondwana Research* **23**,
784 333–353.
785 Vasconcelos C, McKenzie JA, Warthmann R, Bernasconi SM (2005) Calibration of the $\delta^{18}O$
786 paleothermometer for dolomite precipitated in microbial cultures and natural environments. *Geology*
787 **33**, 317–320.

788 Wang HY, Li C, Hu CY, Xie SC (2015) Spurious thermoluminescence characteristics of the Ediacaran
789 Doushantuo Formation (ca. 635-551 Ma) and its implications for marine dissolved organic carbon
790 reservoir. *Journal of Earth Science* **26**, 883–892.
791 Wang X, Jiang G, Shi X, Xiao S (2016) Paired carbonate and organic carbon isotope variations of the
792 Ediacaran Doushantuo Formation from an upper slope section at Siduping, South China. *Precambrian*
793 *Research* **273**, 53–66.
794 Wang J, Li ZX (2003) History of Neoproterozoic rift basins in South China: impli-cations for Rodinia
795 break-up. *Precambrian Research* **122**, 141–158.
796 Xiao S, Muscente AD, Chen L, Zhou C, Schiffbauer JD, Wood AD, Polys NF, Yuan X (2014) The Weng'an
797 biota and the Ediacaran radiation of multicellular eukaryotes. *National Science Review* **1**, 498–520.
798 Yin L, Zhu M, Knoll AH, Yuan X, Zhang J, Hu J (2007) Doushantuo embryos preserved inside diapause
799 egg cysts. *Nature* **446**, 661–663.
800 Yuan X, Chen Z, Xiao S, Zhou C, Hua H (2011) An early Ediacaran assemblage of macroscopic and
801 morphologically differentiated eukaryotes. *Nature* **470**, 390–393.
802 Zhang ZY (1986) New material of filamentous fossil Cyanophytes from the Doushantuo formation (Late
803 Sinian) in the eastern Yangtze Gorges (in Chinese with English abstract). *Chinese Journal of Geology*
804 **27(1),** 30–37.
805 Zhou CM, Xie GW, Xiao SH (2005) New data of microfossils from Doushantuo Formation at
806 Zhangcunping in Yichang, Hubei province (in Chinese with English abstract). *Acta*
807 *Micropalaeontologica Sinica* **22(3)**, 217–224.

Zhu CM, Yuan XL, Xiao SH, Chen Z, Xue YS (2004) Phosphatized fossil assemblage from the Doushantuo Formation in Baokang, Hubei province (in Chinese with English abstract). *Acta Micropalaeontologica Sinica* **21(2)**, 349–366.

Zhu M, Zhang J, Yang A (2007) Integrated Ediacaran (Sinian) chronostratigraphy of South China. *Palaeogeography,Palaeoclimatology, Palaeoecology* **254**, 7–61.

Zhu M, Lu M, Zhang J, Zhao F, Li G, Yang A, Zhao X, Zhao M (2013) Carbon isotope chemostratigraphy and sedimentary facies evolution of the Edi-acaran Doushantuo Formation in western Hubei, South China. *Precambrian Research* **225**, 7–28.

Figure captions:

Figure 1. Geological framework of the Ediacaran Doushantuo Formation in South China. (A) Palaeogeographic reconstruction of the Ediacaran Yangtze Platform (modified from Jiang et al., 2011) showing locations of the three study sections (Zhangcunping, Jiulongwan, Siduping). (B) Proximal-to-distal transect across the Yangtze Platform, showing relative paleodepths of the study sections (after Zhu et al., 2013). Legend: 1, thick-bedded grainstone; 2, micritic dolostone; 3, muddy or silty laminated dolostone; 4, limestone; 5, phosphorite; 6, glaciogenic diamictite; 7, black shale; 8, cherty bands and nodules in the carbonate; 9, carbonate interbeds or lenticular beds; 10, cherty nodules in shale; 11, carbonate concretions; 12, sequence boundary; 13, dark or dark-gray silty shale or mudstone.

Figure 2. C-isotope chemostratigraphy of the Ediacaran Doushantuo Formation at study sections. Data sources include this study (yellow-filled symbols), Li et al. (2010) (red-filled symbols), and McFadden et

al. (2008) (Jiulongwan) and Jiang et al. (2010) (Siduping; both blue-field symbols). Green curves represent five-point running averages for high-resolution intervals (note: raw data used for low-resolution intervals). Gray-shaded areas represent negative excursions of $\delta^{13}C_{carb}$. Three age constraints are from Condon et al. (2005) and Liu et al. (2009). See text for more details on stratigraphic correlations and the "IP" and "EN" event designations for study sections. Abbreviations: NT = Nantuo Formation; DY = Dengying Formation; LCP = Liuchapo Formation.

Figure 3. Mn/Sr and $\delta^{18}O_{carb}$ data of the Ediacaran Doushantuo Formation at study sections. The corresponding $\delta^{13}C_{carb}$ data are given for comparison. Stratigraphic details and abbreviations are identical to those in Figure 2.

Figure 4. Crossplots of $\delta^{13}C_{carb}$ versus $\delta^{18}O_{carb}$ for the negative C-isotope excursion intervals in study sections. (A-C) Data from EN1, EN1-1, EN1-2, EN2 and EN3a-c at Zhangcunping, Jiulongwan, and Siduping sections, respectively. The correlation coefficient (r^2) and t-test p value (where needed) for each C-isotope excursion are shown in the legend. (D) Separation of EN3 data from the three study sections into dolomitic and calcitic samples.

Figure 5. A compilation of Ediacaran Sr isotope data reported from different global sites. Corresponding $\delta^{13}C_{carb}$ records are given for comparison. Sr-isotope data sources: South China, Sawaki et al. (2010); Canada, Narbonne et al. (1994); Oman, Burns and Matter (1993); Australia, Foden et al. (2001). C-isotopic data sources: South China, this study, Tahata et al. (2013), Li et al. (2010), McFadden et al. (2008);

Australia, Calver (2000); Oman: Fike et al. (2006), Siberia, Pokrovskii et al. (2006); Canada, Macdonald et al. (2013). Three age constraints are from Condon et al. (2005).

Figure 6. C-S chemostratigraphy of successions capturing typical Shuram Excursion in South China (A), Mexico (B), southwest USA (C) and Oman (D) where paired carbonate-associated sulfate (CAS) and C-isotope data were reported. Note: all chemostratigraphic data capturing the early onset of the SE (<120 m) in (D) were normalized to a thickness of 120 m based on the base and top surfaces of the Khufai Formation (Osburn et al., 2014) while the > 120-m data capturing the rest of the Shuram Excursion were normalized to a thickness of 240 m in order to match the normalized thickness of <120 m for the Khufai Formation. Data sources: South China, this study and Li et al. (2010); Mexico, Loyd et al. (2012); southwest USA, Kaufman et al. (2007); Oman, Fike et al. (2006) and Osburn et al. (2015).

Figure 7. Schematic presentation of the proposed heterogeneous oxidation model involving greatly enhanced weathering nutrient and sulfate fluxes and coastal surface-ocean oxygenation for interpreting the high spatial heterogeneity of the Shuram Excursion (i.e., the largest negative $\delta^{13}C_{carb}$ excursion of the Ediacaran) as recorded in the upper Doushantuo Formation (EN3) across the Yangtze Platform. See text for more details. Abbreviations: DIC_{rc}= dissolved inorganic carbon derived from local oxidation of subsurface reduced carbon; DIC_{bg}= global marine background of dissolved inorganic carbon.

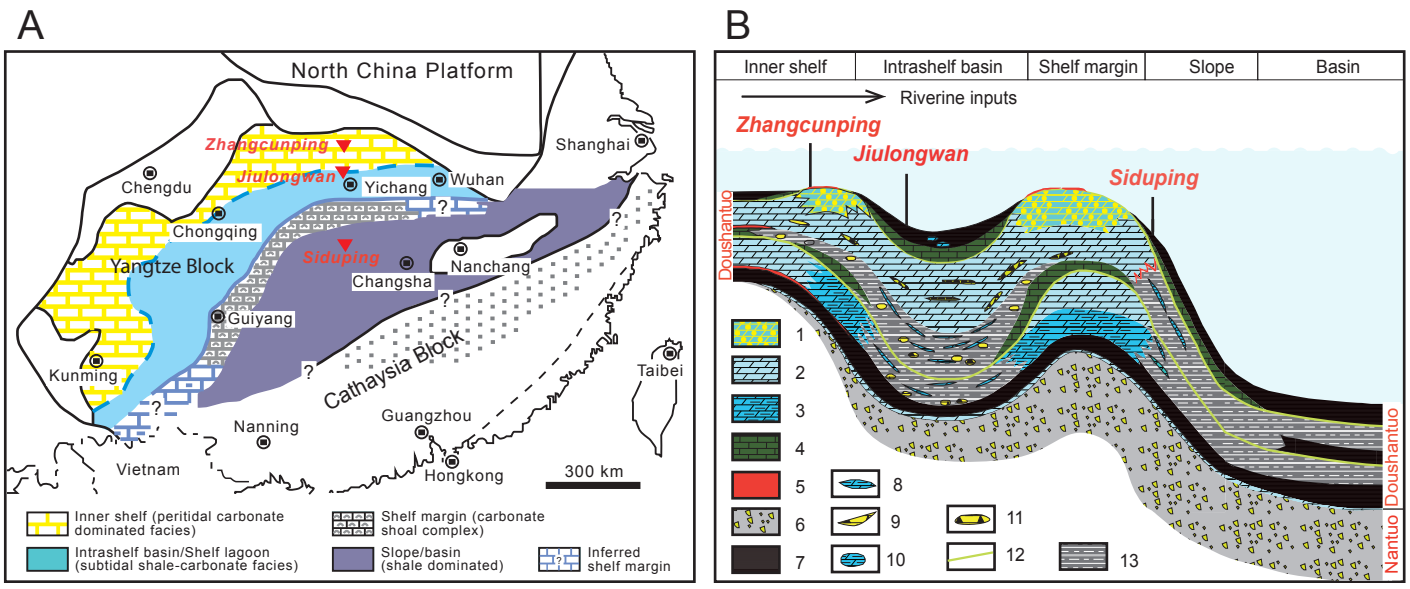
A
North China Platform
Zhangcunping
Jiulongwan
Siduping
Chengdu
Chongqing
Yangtze Block
Guiyang
Kunming
Vietnam
Nanning
Yichang
Wuhan
Changsha
Nanchang
Shanghai
Cathaysia Block
Guangzhou
Hongkong
Taibei
300 km
Inner shelf (peritidal carbonate dominated facies)
Intrashelf basin/Shelf lagoon (subtidal shale-carbonate facies)
Shelf margin (carbonate shoal complex)
Slope/basin (shale dominated)
Inferred shelf margin
B
Inner shelf
Intrashelf basin
Shelf margin
Slope
Basin
Riverine inputs
Zhangcunping
Jiulongwan
Siduping
Doushantuo
Nantuo
1
2
3
4
5
6
7
8
9
10
11
12
13

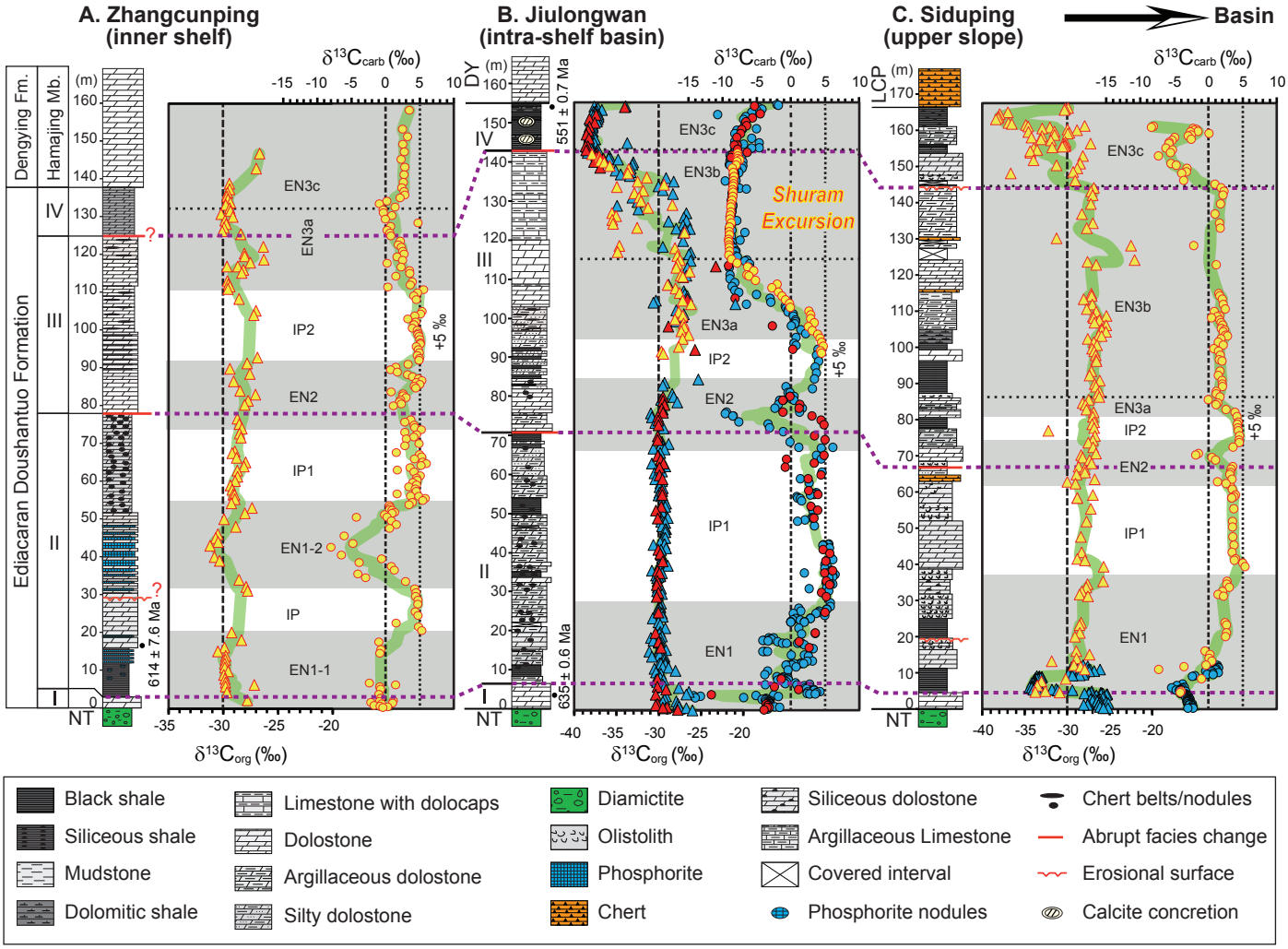
A. Zhangcunping
(inner shelf)
B. Jiulongwan
(intra-shelf basin)
C. Siduping
(upper slope)
Basin
Dengying Fm.
Hamajing Mb.
Ediacaran Doushantuo Formation
δ13Ccarb (‰)
δ13Corg (‰)
(m)
EN3c
EN3b
EN3a
IP2
EN2
IP1
EN1-2
IP
EN1-1
EN1
Shuram
Excursion
+5 ‰
614 ± 7.6 Ma
635 ± 0.6 Ma
551 ± 0.7 Ma
DY
LCP
NT
Black shale
Siliceous shale
Mudstone
Dolomitic shale
Limestone with dolocaps
Dolostone
Argillaceous dolostone
Silty dolostone
Diamictite
Olistolith
Phosphorite
Chert
Siliceous dolostone
Argillaceous Limestone
Covered interval
Phosphorite nodules
Chert belts/nodules
Abrupt facies change
Erosional surface
Calcite concretion

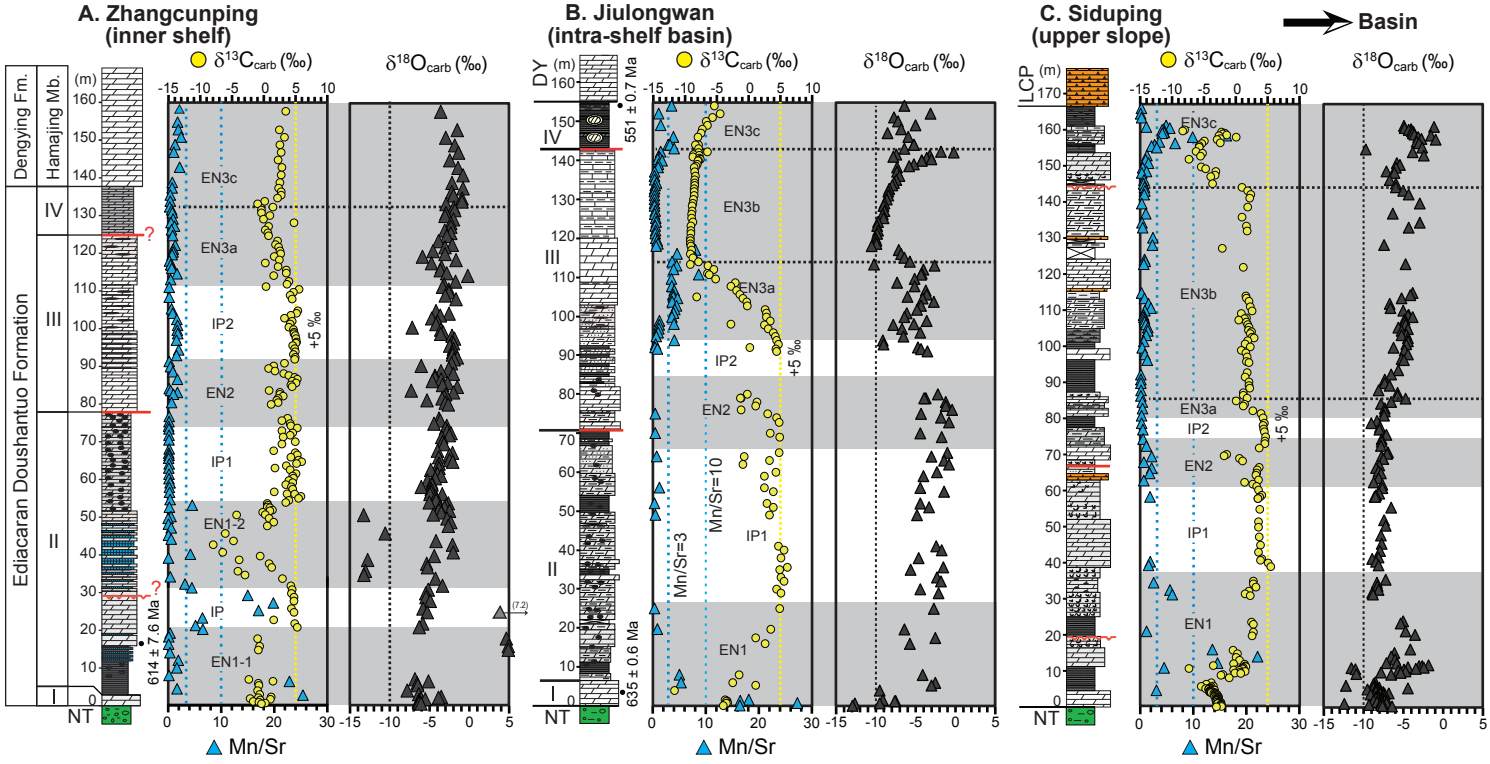
A. Zhangcunping
(inner shelf)
B. Jiulongwan
(intra-shelf basin)
C. Siduping
(upper slope)
Basin
Dengying Fm.
Hamajing Mb.
Ediacaran Doushantuo Formation
δ13Ccarb (‰)
δ18Ocarb (‰)
Mn/Sr
EN3c
EN3b
EN3a
IP2
EN2
IP1
EN1-2
IP
EN1-1
EN1
+5 ‰
Mn/Sr=3
Mn/Sr=10
614 ± 7.6 Ma
635 ± 0.6 Ma
551 ± 0.7 Ma
DY
LCP
NT

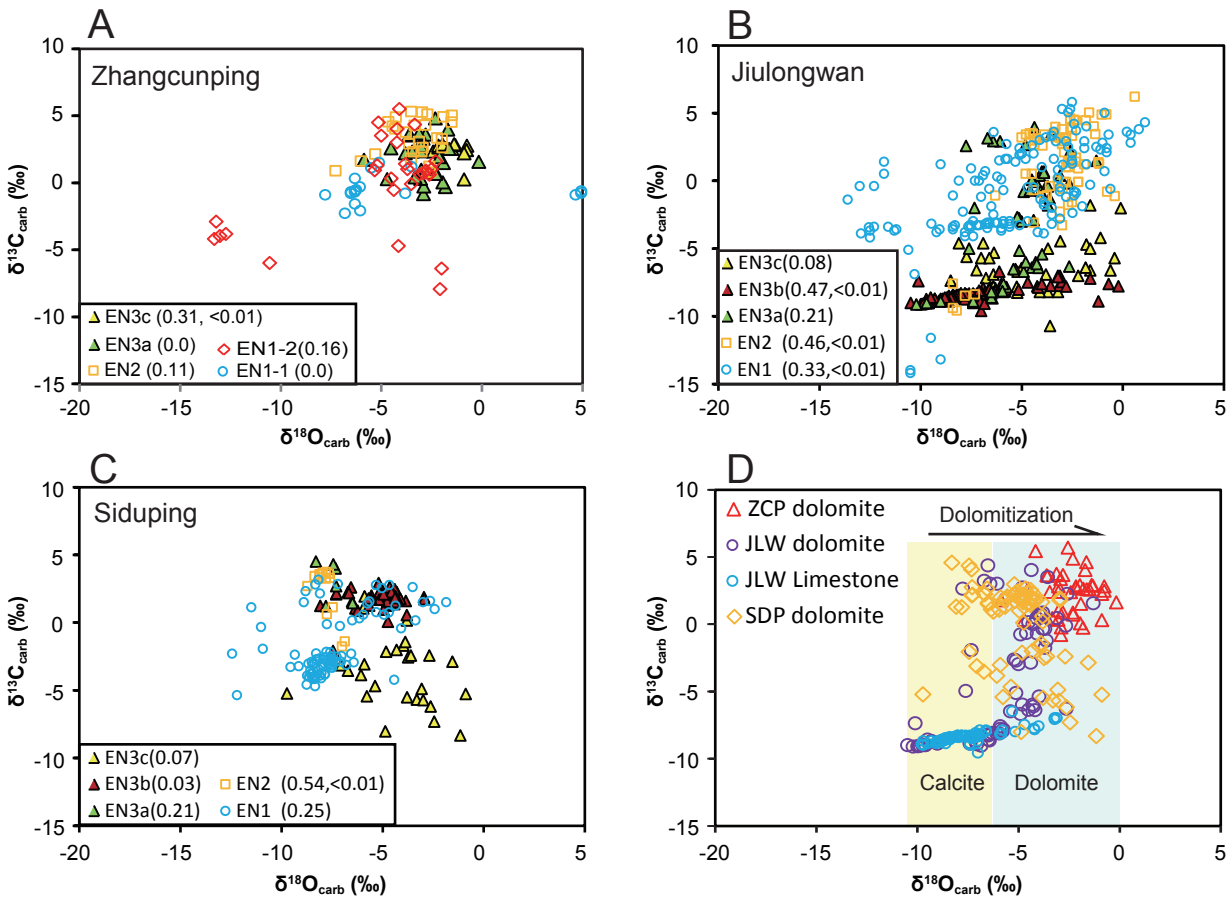
A
Zhangcunping
EN3c (0.31, <0.01)
EN3a (0.0)
EN1-2(0.16)
EN2 (0.11)
EN1-1 (0.0)
B
Jiulongwan
EN3c(0.08)
EN3b(0.47,<0.01)
EN3a(0.21)
EN2 (0.46,<0.01)
EN1 (0.33,<0.01)
C
Siduping
EN3c(0.07)
EN3b(0.03)
EN2 (0.54,<0.01)
EN3a(0.21)
EN1 (0.25)
D
ZCP dolomite
JLW dolomite
JLW Limestone
SDP dolomite
Dolomitization
Calcite
Dolomite
δ13Ccarb (‰)
δ18Ocarb (‰)

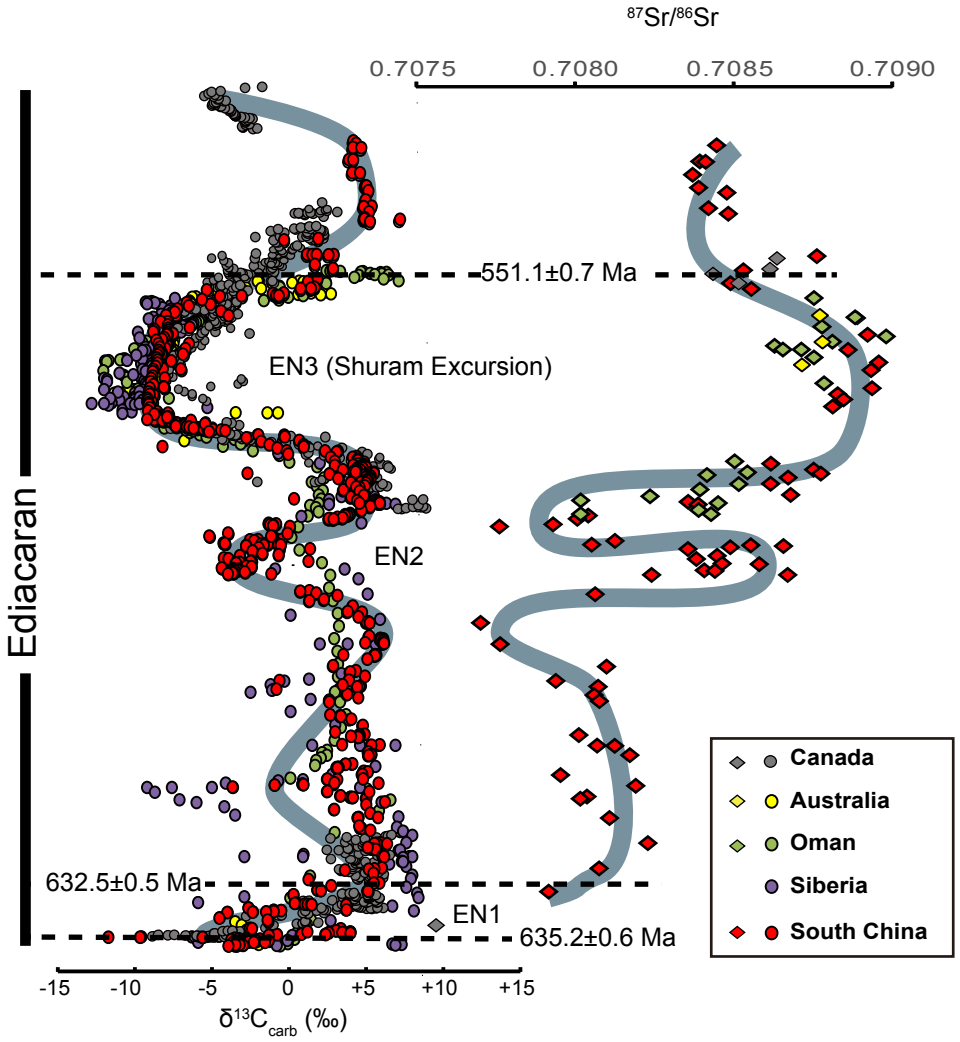
87Sr/86Sr
0.7075
0.7080
0.7085
0.7090
551.1±0.7 Ma
EN3 (Shuram Excursion)
EN2
Ediacaran
632.5±0.5 Ma
EN1
635.2±0.6 Ma
Canada
Australia
Oman
Siberia
South China
-15
-10
-5
0
+5
+10
+15
δ13Ccarb (‰)

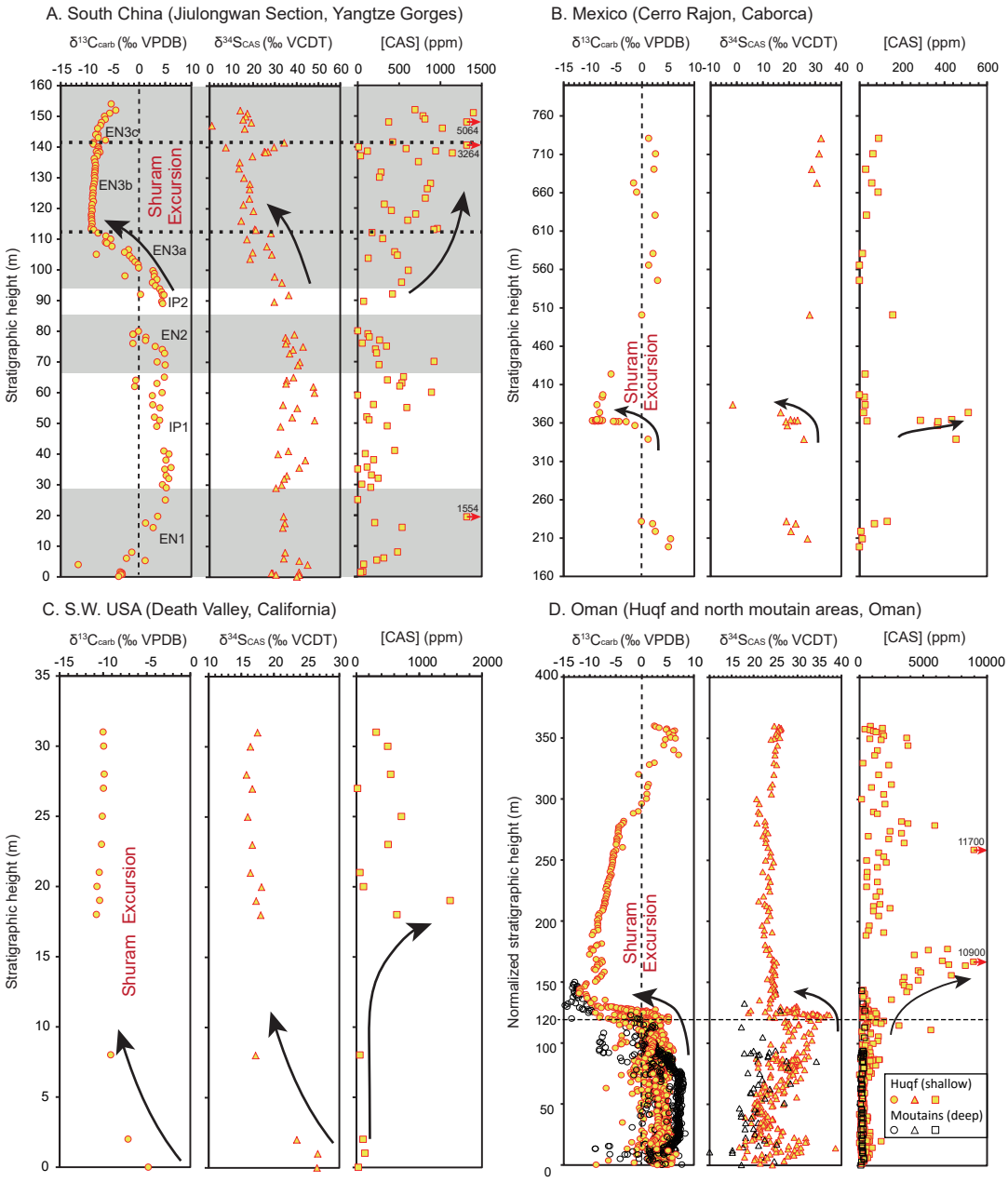
A. South China (Jiulongwan Section, Yangtze Gorges)
δ13Ccarb (‰ VPDB)
δ34SCAS (‰ VCDT)
[CAS] (ppm)
Stratigraphic height (m)
EN3c
EN3b
EN3a
IP2
EN2
IP1
EN1
Shuram Excursion
5064
3264
1554
B. Mexico (Cerro Rajon, Caborca)
δ13Ccarb (‰ VPDB)
δ34SCAS (‰ VCDT)
[CAS] (ppm)
Stratigraphic height (m)
Shuram Excursion
C. S.W. USA (Death Valley, California)
δ13Ccarb (‰ VPDB)
δ34SCAS (‰ VCDT)
[CAS] (ppm)
Stratigraphic height (m)
Shuram Excursion
D. Oman (Huqf and north moutain areas, Oman)
δ13Ccarb (‰ VPDB)
δ34SCAS (‰ VCDT)
[CAS] (ppm)
Normalized stratigraphic height (m)
Shuram Excursion
11700
10900
Huqf (shallow)
Moutains (deep)

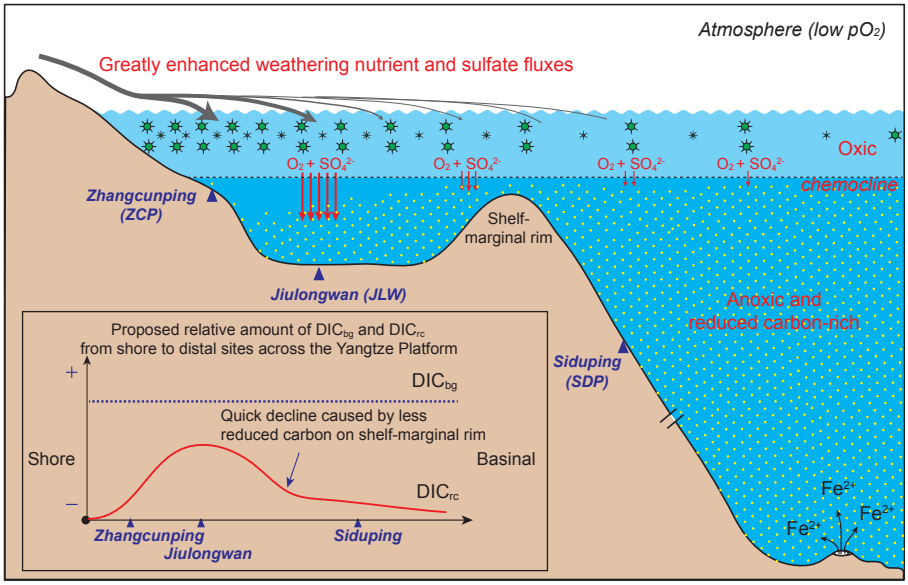
Atmosphere (low pO2)
Greatly enhanced weathering nutrient and sulfate fluxes
O2 + SO4 2-
O2 + SO4 2-
O2 + SO4 2-
O2 + SO4 2-
Oxic
chemocline
Zhangcunping
(ZCP)
Shelf-
marginal rim
Jiulongwan (JLW)
Anoxic and
reduced carbon-rich
Siduping
(SDP)
Proposed relative amount of DICbg and DICrc
from shore to distal sites across the Yangtze Platform
+
DICbg
Quick decline caused by less
reduced carbon on shelf-marginal rim
Shore
Basinal
DICrc
−
Zhangcunping
Jiulongwan
Siduping
Fe2+
Fe2+
Fe2+

Supplementary Information for:

Uncovering the spatial heterogeneity of Ediacaran carbon cycling

Chao Li, Dalton S. Hardisty, Genming Luo, Junhua Huang, Thomas J. Algeo, Meng Cheng, Wei Shi, Zhihui An, Jinnan Tong, Shucheng Xie, Nianzhi Jiao, Timothy W. Lyons

Table S1. A summary of geochemical data of the study sections.

Sample	Depth (m above Nantuo Fm.)	Mn/Sr	TOC (wt %)	TIC (wt %)	$\delta^{13}C_{carb}$ (‰ VPDB)	$\delta^{13}C_{org}$ (‰ VPDB)	$\triangle^{13}C$ (‰ VPDB)	$\delta^{18}O$ (‰ VPDB)	$\delta^{34}S_{CAS}$ (‰ VPDB)	[CAS] (ppm)
1. Zhangcunping Section (Inner shelf facies)										
ZK312-265	157.7	1.94	0.03	12.1	3.5			-3.5		
ZK312-266	154.76	1.82	0.02	12.1						
ZK312-267	152.76	1.96	0.01	13.1	2.5			-1.5		
ZK312-268	150.76	2.47	0.01	12.3	3.3			-2.9		
ZK312-269	148.76	1.33	0.03	12.3	2.6			-1.8		
ZK312-270	146.76	1.09	0.03	12.2	2.8	-26.7	29.5	-1.3		
ZK312-271	144.76		0.01	13.2	2.3			-2.4		
ZK312-272	142.76	2.2	0.48	12.3	2.9	-27	29.8	-1.4		
ZK312-273	140.76		0.02	12	2.8			-0.7		
ZK312-274	138.76	0.83	0.45	11.6	2.6	-29.4	32	-2.1		
ZK312-275	137.29	0.79	0.36	11.7	2.4	-29.4	31.8	-0.8		
ZK312-276	136.33		0.93	10.9	2.8	-29.6	32.4	-2.2		
ZK312-277	135.38	0.45	1.07	10.6	2.8	-29.7	32.5	-2		
ZK312-278	134.62				2.2	-29.6	31.7	-0.9		
ZK312-279	133.76	0.45	0.28	12.8	0.2	-29.3	29.6	-0.9		
ZK312-280	133.1				-0.9	-29.8	28.9	-2.9		
ZK312-281	132.24	0.33	0.2	8.3	1.5	-29.4	30.9	-1.9		
ZK312-282	131.49	0.72			-0.3	-29.3	29	-1.8		
ZK312-283	130.73	0.81	0.84	11.6	-0.3	-30.2	29.9	-2.9		
ZK312-284	129.97				1	-29.1	30.1	-3		

ZK312-285	129.01	0.97	0.5	11.8	0	-29.8	29.8	-1.9
ZK312-286	128.06	0.59	0.37	12.3	4.8	-29.7	34.5	-2.3
ZK312-287	127.1	1.22			0.8	-29.9	30.7	-2.3
ZK312-288	126.14	0.67	0.55	11.9	0.3	-30.1	30.4	-3
ZK312-289	125.38				0.7	-28.4	29.1	-2.3
ZK312-290	124.62	0.9	0.02	12.2	0.8			-2.8
ZK312-291	123.67				2.2			-3.8
ZK312-292	122.71				1.9			-2.1
ZK312-293	122.05	1.36	0.04	12.6	2.4	-26.3	28.7	-3
ZK312-294	121.05	0.98	0.04	12.7	2.6			-4.5
ZK312-295	120.25	0.97	0.09	12.4	2.7	-28.1	30.8	-3
ZK312-296	119.55	0.79			1.7	-28	29.8	-5.9
ZK312-297	118.65				2.5	-26.3	28.8	-1.6
ZK312-298	117.85	0.31	0.05	12.8	0.3	-27.5	27.8	-4.7
ZK312-299-1	116.85	0.68	0.13	11.9	2.3	-28.7	31	-3.5
ZK312-299-2	116.85	0.53		9.4		-29.7		
ZK312-300	115.95	0.71	0.11	10.8	3.6	-28.1	31.7	-3.6
ZK312-301	115.15				3.6	-28.3	31.9	-2.8
ZK312-302	114.45	1.73	0.01	12.6	1.6			-0.2
ZK312-303	113.55							
ZK312-304	112.95	0.5	1.02	11	4	-29.6	33.6	-1.7
ZK312-305	112.15				3.7	-29.5	33.2	-3.1
ZK312-306	111.55				0.4	-29.4	29.8	-3.3
ZK312-307	110.85	0.25	0.69	10.9	5.6	-29.6	35.2	-2.5
ZK312-308	110.05				4.7			-2.5
ZK312-309	109.25				4.2			-3
ZK312-310	108.25	0.25			4.5	-28.6	33.1	-1.6
ZK312-311	105.15	0.69			5.4	-27	32.4	-4.1
ZK312-312	104.45				5.2			-2.5
ZK312-313	103.95	0.88	0.11	12.5	4.3	-27.2	31.5	-3.6
ZK312-314	103.15				3.3			-4.7
ZK312-315	102.35	1.67	0.06	12.7	4.5			-4
ZK312-316	101.65				4.2			-4.1
ZK312-317	100.75	1.82	0.02	12.6	4			-7.1
ZK312-318	100.15				4.7			-3.6
ZK312-319	99.45	1.75	0.02	12	4.8			-3.2
ZK312-320	99.05				4.8			-3.5
ZK312-321	98.55	1.86	0.03	12.3	5			-2.1
ZK312-322	97.75				5.1			-1.8
ZK312-323	96.85	1.6	0.04	11.8	5.2			-2.1
ZK312-324	96.55				5.1			-1.9
ZK312-325	95.9				4.6			-2.4
ZK312-326	95.05				4.9			-2
ZK312-327	94.25	2.02	0.02	12.1	5			-2.1
ZK312-328	93.55				4.7			-2.1

ZK312-329	92.75	1.63	0.05	10.9	5	-26.9	31.9	-1.5
ZK312-330	92.25				4.9			-1.9
ZK312-331	91.19	0.23	0.13	7	3.3	-27.8	31.1	-2.2
ZK312-332	90.49				1.6			-6
ZK312-333	89.79	0.48	1.03	6.8	0.8	-29.4	30.2	-2.6
ZK312-334	89.15				1.8			-3.5
ZK312-335	88.45	0.94	0.25	9.6	3.2	-27.6	30.8	-2
ZK312-336	87.95				4			-4.3
ZK312-337	87.45		0.07	11.7	4.9			-4.3
ZK312-338	86.95				5.3			-3.5
ZK312-339	86.45	1.78	0.23	11.7	4.5	-29	33.6	-4.6
ZK312-340	85.95				5.1			-2.7
ZK312-341	85.45		0.04	9.4	4.3			-3.3
ZK312-342	84.95				4.5			-1.5
ZK312-344	83.95	0.23	0.34	3.8	0.9	-28.5	29.3	-7.3
ZK312-345	83.45	0.5	0.12	6.3	2.6			-2
ZK312-346	82.95	1.78			2.6	-27	29.6	-2.9
ZK312-347	82.45	1.02	0.06	8.8	3.1			-3.1
ZK312-348	81.85				2.3			-3.4
ZK312-349	81.35		0.05	12.1	2.1	-27.7	29.8	-5.3
ZK312-350	80.75				2.3			-3
ZK312-351	80.25	0.67	0.1	10.1	1.2	-28	29.2	-2.6
ZK312-356	76.57	0.23	1.38	4.9	3.8	-28.7	32.5	-3.8
ZK312-357	75.97				2.9			-3.6
ZK312-358	75.17	0.22	1.31	5.2	4.2	-28.5	32.7	-4.4
ZK312-359	74.57				4.3			-2.8
ZK312-360	73.97	0.14	0.91	5.9	5.3	-28.3	33.5	-3
ZK312-361	73.27	0.21	0.9	6.1	2.9			-2.7
ZK312-362	72.67		1.22	4.4	4.6	-28.5	33.1	-2.3
ZK312-363	72.07		1.38	5.6	4.2			-2.5
ZK312-364	71.57	0.21	1.32	4.9	3.1	-28.4	31.4	-3.4
ZK312-365	70.34	0.21	1.33	5.4	5			-3.3
ZK312-366	69.74		0.2	0.6	2.9			-3.1
ZK312-368	67.94	0.24	0.34	10	1.6	-28.9	30.5	-4
ZK312-370	67.44		0.66	8.2	5	-29.2	34.2	-2.1
ZK312-371	66.84	0.17	0.94	5.5	5.3			-2.5
ZK312-372	66.24	0.19	0.55	8.9	4.3	-28.8	33	-3.8
ZK312-373	65.45	0.15	1.07	4.7	5.5			-2.5
ZK312-374	65.05				6	-27.9	33.9	-2.1
ZK312-375	64.55				5.2			-3.8
ZK312-376	63.95	0.23	0.3	8.6	3.6	-28.1	31.7	-3.9
ZK312-377	63.35				1.8			-3.8
ZK312-378	62.85	0.17	0.47	6.5	4.2	-28.7	32.9	-4.8
ZK312-379	61.85				5.1			-4
ZK312-380	61.25	0.22	1.4	6.3	4.6	-28.7	33.3	-3.5

ZK312-381	60.65				4.7			-4.3
ZK312-382	60.05	0.22			4	-28.9	32.9	-5.2
ZK312-383	59.45				4.6			-4.7
ZK312-384	58.95	0.42	1.7	9	3.5	-29.3	32.8	-4.7
ZK312-385	58.35				4.4			-6
ZK312-386	57.75	0.27	1.33	6.9	4.6	-29.2	33.7	-4.8
ZK312-387	57.05				1.7			-4.8
P312-1	56.48		0.83	7.8	3.7	-29.1	32.8	-3.4
ZK312-388	56.45	0.32	1.21	7.5	4.9	-28.9	33.8	-4.9
ZK312-389	55.85				5.9			-4.2
ZK312-390	55.29				5.5	-28.9	34.4	-4.1
ZK312-391	54.79				4			-4.2
P312-5	54.48	0.42	0.95	2.8				
ZK312-392	54.19		0.68	7.4	3.5	-29.2	32.7	-5
P312-6	53.98				0.6			-2.6
ZK312-393	53.49				0.7			-2.9
P312-8	52.98	4.57	0.13	6.3	0.6	-27.4	28	-3.1
ZK312-394	52.79		0.1	8.4	1			-3.7
P312-9	52.48	0.28	0.09	4				
ZK312-395	52.19				1.4			-3.8
P312-10	51.98				1			-2.5
ZK312-396	51.59		0.1	7.4	-0.1	-28	27.9	-3.5
P312-12	50.98				0.3			-4.5
ZK312-397	50.89				-4.2			-13.3
P312-13	50.48		0.07	1.4				
P312-14	49.98	0.58			0.9	-29.9	30.8	-2.8
P312-15	49.48	0.04						
P312-16	48.98				1.6			-2.3
P312-17	48.48		0.02	1.1				
P312-18	47.98	0.11			0.6	-28.8	29.5	-2.6
P312-20	46.98	0.63	0.02	7.4				
P312-22	45.98				-6	-30.5	24.5	-10.6
P312-24	44.98	0.09	0.47	0.7		-30.7		
P312-26	43.98	0.62			-4.7	-30.5	25.7	-4.1
P312-28	42.98				-7.9	-31.2	23.3	-2.1
P312-30	40.96				-6.4			-2
P312-32	39.96	4.23	0.12	9.3	-0.5	-30.8	30.3	-4.4
P312-34	38.96	0.09	0.16	0.6	-3.8	-30.3	26.5	-12.7
P312-36	37.96		0.01	11.6	0.9			-5.3
P312-38	36.96				1.3			-5.2
P312-40	35.96		0.09	0.3	-4			-13
P312-42	34.96				-2.9			-13.2
P312-44	33.96	0.46	0.06	2.2	3	-28.5	31.5	-4.2
P312-46	32.05	3.21			4.3	-27.9	32.2	-3.3
P312-48	31.05	4.51	0.02	9	4.5	-27.8	32.3	-5.1

P312-50	30.05				4.4			-5.4		
P312-52	29.03	15.03	0.01	11.9	4.8			-5.4		
P312-54	28.03				4.8			-4.9		
P312-56	27.03	19.83	0.01	12.2						
P312-58	26.03				4.4			-5.8		
P312-60	25.03	17.07	0.01	11.9	4.8			-5.3		
P312-64	23.03	6.51	0.02	11.3	1.6			7.2		
P312-66	22.03				4.9			-5.8		
P312-68	21.03	5.18	0.02	11.4	5.3			-6.3		
P312-70	20.03	6.58				-29.2	29.2			
P312-72	19.03	0.4	0.05	0.3						
P312-74	18.03	0.17	0.05	0.4	-0.9	-28.3	27.4	4.7		
P312-76	17.03		0.05	0.4						
P312-78	16.03	0.13	0.67	0.3	-0.6	-29.9	29.2	4.9		
P312-80	15.03		0.83	0.1	-0.8	-30.5	29.7	4.9		
P312-82	13.8	0.39	0.94	0		-29.8	29.8			
P312-84	12.8		0.95	0.1		-29.8	29.8			
P312-86	11.8	1.95	0.98	0		-29.9	29.9			
P312-88	10.78		1.14	0		-29.8	29.8			
P312-90	9.78	1.7	0.88	0.1		-29.5	29.5			
P312-92	8.78		1.22	0.1		-30	30			
P312-94	7.78	0.21	0.69	0.2		-29.8	29.8			
ZK312-398	7.2		0.13	1.2	-2.3			-6.8		
P312-96	6.78		0.89	0.1		-29.8				
ZK312-399	6.7				1.5			-5.1		
ZK312-400	6.2	22.88			-0.8	-27.2	26.4	-6.5		
P312-98	5.78		0.83	0.1		-29.8				
ZK312-401	5.6				-0.7			-6.5		
P312-101	4.24	1.72	0.91	0	-0.9	-29.6	28.7	-7.8		
P312-103	2.8				-0.6			-6.3		
P312-105	2.1	25.44	0.02	11.9	1.2			-3.5		
P312-106	1.9				-0.8			-3.8		
P312-107	1.7				-2.1	-27.8	25.7	-6		
P312-108	1.5				1.1			-5.5		
P312-109	1.3		0.02	11.4	-0.5			-6.2		
P312-111	0.9				-1.6			-6.3		
P312-112	0.7				-0.7			-6.3		
P312-113	0.5				0.3			-6.3		
P312-114	0.3		0.02	11.8	-0.3			-6		

2. Jiulongwan Section (Intra-shelf-basin facies)

HN-23	154	3.53	15.1	1.1	-5.3	-34	28.7	-6.4		
HN-21	152	1.1	5.2	3.7	-4.4	-37.4	33	-3.1	14.2	694.1

HN-20	151			1	-5.6	-38.2	32.6	-7.7	17.4	1399.2
HN-19	150			1.4	-6.6	-37.5	31	-7.2	16.7	789.4
HN-18	149	1.49	6.4	1.6	-6.4	-38.2	31.7	-5	15.5	813.8
HN-17	148			1.3	-7.2	-38.3	31.2	-6.8	19.2	375.7
HN-16	147			0.5	-7.4	-38.5	31.2	-8.5	1.1	5064
HN-15	146	3.89	5	1.8	-7.9	-38.2	30.3	-5.9	16.2	1025.3
HN-13	144	2.9	4.8	1.1	-7.8	-38.4	30.6	-5.2		
HN-09	144	3.22	4.6	0.9	-8.3	-38.6	30.4	-5.2		
HN-12	143	4.03	5.1	0.8	-7.8	-38.6	30.8	-6.4		
HN-11	142.2	1.47	2	0.6	-6.4	-37.4	31	-1.8		
JLW-01	142	8.56	1	10.4	-7.8	-37.9	30.1	-0.2	7.5	423.5
HN-08	141.5		0.2	11	-8.6	-37.3	28.7	-7.4	34.3	3263.9
JLW-02	141.3		0.4	10.5	-7.7	-37	29.3	-3.2		
HN-10	140.9	1.17	0.3	10.8	-8.7	-36.5	27.8	-7.8		12.4
JLW-03	140.6	1.36	0.4	10.6	-7.7	-37	29.2	-3.6	25.2	587
JLW-04	140.3	0.94	0.4	11.9	-7.5	-36.9	29.4	-3	25.7	942.5
HN-06	140		0.2	10.6	-7.8	-37.6	29.9	-4.2	29.7	118.4
JLW-05	139.9	1.76	0.5	9.5	-7.9	-36.4	28.6	-4.2		
JLW-06	139	1.05	0.2	10.5	-8	-35.8	27.8	-5.2	19.7	1146.1
HN-07	138.5		0.1	10.8	-8.2	-36.9	28.8	-5.8	26.9	36.1
JLW-07	138.2	1.01	0.1	11.2	-8.5	-33.5	25	-7.3		
JLW-08	137.1	0.33	0.1	10.4	-8.4	-33.7	25.3	-7.3	13.9	735.5
JLW-09	136	0.31	0	11.4	-8.3	-31.4	23.1	-7		
JLW-10	135	0.34			-8.4	-32.5	24.1	-7.4	13.5	
JLW-11	134.2	0.67	0.1	10.5	-8.4	-29.4	21	-7.7		
JLW-12	133.6	0.45	0.3	10.1	-8.4	-34.9	26.5	-7.9		283.7
JLW-13	132.7	0.33	0.1	11.1	-8.5	-31.8	23.3	-8.3		
JLW-14	132	0.27	-0.7	11.4	-8.5	-32.9	24.4	-8.4	15.8	263.7
JLW-15	131	0.29	0	11.1	-8.5	-32.3	23.8	-8.4		
JLW-16	130	0.3	0.4	10.1	-8.6	-32.1	23.5	-8.6	18.5	883
JLW-17	129	0.31	0	10.6	-8.7	-28.4	19.6	-8.9		
JLW-18	128.3	0.31	-1.1	11.3	-8.8	-31.2	22.5	-9	18.4	843
JLW-19	127	0.45	0.1	12.2	-8.8	-35.5	26.7	-8.9		
JLW-20	126.2	0.35	1.4	10.8	-8.9	-35	26.2	-9.1		
JLW-21	125.2	0.54	0.1	10.1	-8.9	-35.5	26.6	-9	18.4	818.6
JLW-22	124.2	0.6	1.1	10.3	-8.7	-35.4	26.7	-9.7		
JLW-23	123.2	0.44	0	10.5	-9	-32.5	23.6	-9.8	15.5	323.3
JLW-24	122	0.51	1.5	9.6	-9	-26.9	17.9	-9.7		
JLW-25	121.2	0.45	0	10.5	-9			-9.8	20.2	409.1
JLW-26	120	0.56	0	10.2	-9.1			-10		703.2
JLW-27	119.4	0.82	0	11.7	-9.1			-9.9		
JLW-28	118.6	0.95	0.9	10	-9.1	-34.7	25.6	-9.9		
JLW-29	118	0.62	0	10.4	-9	-28.1	19.1	-10.5	14.6	606.2
JLW-30	117	8.04	0.5	10.5	-8.9	-34.8	25.9	-7.1		

JLW-31	116	4.56	0	11.1	-9.1	-27.8	18.7	-6.8		
JLW-32	115	7.98	2.7	8.5	-8.7	-27.5	18.8	-6.4	21.3	965.9
JLW-33	114	3.65	0	10.1	-7.8	-27.8	19.9	-5.7	28.3	921.7
HN-05	113.3		0.2	10.3	-9.1	-23.2	14.1	-10.2	20.8	173.8
JLW-34	113	4.5	1.6	10.3	-6.3	-27.9	21.6	-2.6		
JLW-35	112	3.93	0	11.6	-5.4	-26.3	20.9	-4	17.2	303.6
JLW-36	111		2.5	8.9	-6.4	-27.4	21	-4.2		
JLW-37	110.7	8.69	0	9.8	-6.1	-27.1	21	-4.3		
JLW-38	109.6	3.5	2.5	12.2	-5.1			-5.1	26.3	
JLW-39	108.6		0.1	3.5	-2	-28.9	26.9	-7.3		
JLW-40	107.7	3.57	0	14.2	-2.7	-28	25.2	-5.1	19.9	448.7
JLW-41	106.6	4.02	1.1	11.7	-1.8	-27.5	25.7	-3.7		
JLW-42	105.6	3.83	0.1	11.6	-1.3			-3.6	18.6	480.7
HN-04	105	3.86	0	9.6	-8.1	-26.6	18.4	-6	28.6	127.6
JLW-43	104.6	4.67	3.6	10.2	-0.8	-27.2	26.4	-4.1		
JLW-44	103.7	3.66	0	11.2	-0.2	-26.2	26	-2.7		
JLW-45	102.7	4.47	1.7	12	-0.1			-4.3		
JLW-46	101.7	4.17	0.1	10.4	2.7	-27.6	30.3	-4.8		612.9
JLW-47	100.8	3.93	2.7	10.4	2.9	-27.1	30.1	-6.1		
JLW-48	99.8	3.62	0.1	12	2.9	-28.1	31	-6.4	29.9	
JLW-49	98.8	1.25	2.3	8.9	3.5	-27	30.5	-3.6		
HN-02	98	4	0	12.3	-2.7	-28.8	26.2	-5.2		
JLW-50	97.8	1.21	0.1	11.2	2.6	-27	29.6	-7.8	33.3	530.5
JLW-51	96.8	1.14	0.1	11.8	3.2	-27.3	30.5	-6.7		
JLW-52	95.8	1	0.1	11.1	4	-26.4	30.4	-4.4		
JLW-53	94.8	0.64			4.3	-27.2	31.5	-6.5		
JLW-54	93.8	4.05	0.1	9.2	4.5			-9.1	36.4	422.7
JLW-55	92.8	0.51	1.4	10.8	4.8	-27.6	32.4	-9		
HN-01	92	0.42	0	11.8	0.3	-25.7	26	-4.7		
JLW-56	91.6	0.86	0.4	10.7	4.4	-29.6	34	-4.3	29.7	73.9
JLW-57	91		2.1	10.6	4.5	-29.5	34	-3.5		
JS-69	80			6	-0.1	-29.5	29.4	-2.2		0
JS-68O	79		0.7	6.4	-1.1			-3.7		
JS-68I	79		0.8	6.2	-1.2	-29.5	28.3	-3.9	39	123.9
JS-67	78			5.9	1.4	-29.3	30.6	-1.2	34.9	141.8
JS-66	77			4.2	1.2	-29.6	30.9	-1.2	35.6	266.3
JS-65	76			7.1	-1.1	-29.5	28.3	-0.4	35.1	56.3
JS-64	75	0.45	1.6	6.2	3.1	-30.1	33.2	-4.3	43	348.2
JS-63	74			5	4.5	-30	34.5	-1.8	38.4	216.2
JS-62	72.8			6.9	4.9	-30	34.9	-0.8	36.8	229.7
JS-60	70	0.44	1.6	5.3	3.5	-30.1	33.6	-4.4	41.5	922.6
JS-59	69			7.6	5	-30.1	35.1	-1.7	40.6	259.7
JS-57	65			5.7	4.9	-30.1	35	-1	38.6	555.4
JS-56	64	0.72	0.6	6	-0.6	-29.7	29.1	-3	35.4	361

JS-55	63			5.5	3.4	-29.4	32.9	-1.4	35.2	535.4
JS-54	62			5.8	-0.8	-29.9	29.1	-0.8	47.7	510
JS-52	60			6.5	4.4	-29.9	34.3	-2.3	48.2	891.9
JS-51	59		0.6	7.6	2.6	-29.5	32.1	-4		0
JS-48	56	1.24	1	7.1	2.6	-29.6	32.2	-4.4	33.8	192.3
JS-47	55			5.6	4	-29.6	33.6	-1.4	40.3	595.5
JS-45	52	0.31	0.7	7.9	3	-29.7	32.6	-4.4	38	111.2
JS-44	51			7.7	4	-30.3	34.3	-3.3	48.3	138.1
JS-42	49	0.49	0.9	6.4	3.4	-30.1	33.5	-4.8	32.6	357
JS-40	41		1.1	5.9	4.8	-30	34.8	-2.4	36.2	448.1
JS-39	40			6.7	5.7	-29.8	35.5	-1.7	31.5	93.7
JS-37	38		0.8	5.8	5.2	-29.5	34.6	-4.6	44	193.7
JS-35	35.6			8	6.2	-30.1	36.3	-1.5	41.2	114
JS-34	35		0.9	5.8	5	-29.9	34.8	-5.6		0
JS-32	33			5.7	5.2	-30.1	35.3	-2.3	35.5	167.8
JS-31	32			5.9	5.7	-30.2	35.9	-1.8	34.3	247.7
JS-29	30		1.2	5.8	4.5	-30	34.5	-4.4	33.2	50.5
JS-28	29			5.9	5.2	-30.2	35.4	-2.1	30.5	159.3
JS-26	25	0.32	0.7	7.4	5	-30	35.1	-2.7		0
JS-24	19.7	0.85	2.9	4.2	3.6	-30.4	34	-6.4	34	1554.3
JS-22	17.5			7.5	1.2	-30	31.2	-2.5	34.6	206.2
JS-21	16		1.8	5.5	2.7	-29.7	32.4	-5.7	33.7	538.7
JS-18	8	5.01	1.2	6.5	-1.4	-30.1	28.7	-4.1	34.7	483.1
JS-17	6	5.34	0.5	7.1	-2.4	-30.1	27.8	-2.5	34.1	316.9
JS-15	5.3		0.1	7.4	1.2	-29.1	30.3	-3	41.2	230.8
JS-16	4		0	9.7	-11.6	-30.3	18.7	-9.5	45.1	73.7
HJ-02	1.6	18.15	0.2	11.6	-3.6	-30.1	26.5	-9.1	41.1	64.4
HJ-03	1.3	16.53	0	12	-3.3	-30.4	27.1	-7.5	29	37.7
JS-12	1.25		0	10.1	-3.4			-7.6	28.4	
JS-13	0.75		0.2	11.8	-3.2	-29	25.8	-9.5	30.5	
HJ-01	0.7	27.32	0	11.7	-3.4	-29.5	26.1	-12.6	41.2	
JS-14	0.1	16.46	0.5	9.5	-3.9	-27.7	23.8	-12.9	40.1	

3. Siduping Section (Upper slope facies)

SDP-154	166.1					-29.9				
SDP-155	165.9	0.28				-30.2				
SDP-156	165.5					-30.3				
SDP-159	164.9					-37				
SDP-160	164.4	0.15				-37.9				
SDP-161	163.7					-38				
SDP-162	163.3	0.32				-38.1				
SDP-163	162.9					-38.4				
SDP-165	162					-36.9				

SDP-166	161.7					-36.5		
SDP-167	161.4					-34.8		
SDP-168	161.1	4.93				-27.9		
SDP-169	161		0.1	13.2	-8	-34.6	26.5	-4.9
SDP-170	160.7	1.21			-8.3	-32	23.7	-1.1
SDP-171	160.4	5.61	0.2	12.3	-2.2	-32.9	30.8	-4.8
SDP-172	160.1	4.45	0.1	10.7	-1.7	-30	28.3	-4
SDP-173	159.9	4.15	0	11.3	-2	-28.8	26.8	-4.3
SDP-174	159.6		0.1	7.3	-1.4	-31.5	30	-3.9
SDP-175	159.4	4.5	0	10.3	-2.6	-34.6	32	-3.7
SDP-176	159.2	4.53				-29.8		
SDP-177	159	4.19	0.1	4	0.1	-29.9	30.1	-3.8
SDP-178	158.6		0.1	11.2	-2.4	-31.5	29	-3.6
SDP-179	158.3	16.24	0.3	12.1	-2.9	-33	30.1	-1.5
SDP-180	157.9	9.93	0.2	10.3	-4.9	-34.2	29.3	-3.1
SDP-181	157.4		0.3	12.2	-2.4	-33.1	30.6	-2.7
SDP-182	157.2		0.1	13.3	-5.3	-31.9	26.6	-0.9
SDP-183	156.6	3.64	0.1	11.4	-5.7	-30.2	24.5	-3.3
SDP-184	156.2	6.62	0.4	9.9	-5.7	-27.3	21.5	-3
SDP-185	156					-30.5		
SDP-186	155.8	2.74				-30.2		
SDP-187	155.7					-30.2		
SDP-188	155.6					-30.2		
SDP-189	155.5					-30.4		
SDP-190	155.4	2.15				-30.6		
SDP-191	155.2					-31.8		
SDP-192	155	3.15	0.4	12.5	-6.2	-33.9	27.7	-2.6
SDP-193	154.5		1.2	1.7	-5.2	-33.5	28.3	-9.7
SDP-194-2	154.1		1.5	11.1		-34.3		
SDP-194	153.7		1.5	11.1	-5.5	-34.3	28.8	-3.8
SDP-195	152.8	1.29	0.1	11.5	-7.3	-28.1	20.8	-2.4
SDP-196	151.6	1.07				-34		
SDP-197	150.7	1.6	0.2	11.3	-5.4	-28.5	23	-5.8
SDP-198	150.2		2.8	10.1	-4.7	-31.3	26.6	-5.4
SDP-199	149.4	0.51	0.1	11.6	-3.1	-28.8	25.7	-5.9
SDP-200	148.4	1.24	0.3	11.6	-3.2	-29.3	26.1	-7.1
SDP-201	148	0.34	0.1	4	-3.9	-36.6	32.7	-6.1
SDP-202	146	0.77	0.1	7.7	-3.6	-29	25.5	-6.7
SDP-215	145	0.69	0.1	11.5	1			-5.9
SDP-214	144	0.86	0.1	9.9	1.9	-26.9	28.8	-5.9
SDP-213	143	0.93	0.2	9.3	2.4	-27.2	29.6	-5
SDP-212	142	0.8	0.1	9.2	2.2	-27	29.2	-4.3
SDP-211	139.5	0.34	0.1	10	1.9	-27.2	29.1	-2.9
SDP-210	136.7	1.11	0.1	12.6	1	-28.3	29.3	-6.3

SDP-209	134.2	0.38	0.1	9.2	1.7	-27	28.7	-2.9
SDP-208	132.8	0.51	0.2	10.1	1.8	-27.7	29.6	-4.3
SDP-207	130	2.43	0	11.3		-31.3		
SDP-206	128	2.34	0.1	12.3	-2.1	-22.5	20.4	-7.4
SDP-205	124	0.84				-22.1		
SDP-204	123.5	1.01				-27.6		
SDP-203	122.7	0.72			1.2	-26.6	27.8	-4.7
SDP-143	114.7	0.31	0.1	8.6	1.6	-27.1	28.7	-3.8
SDP-142	114.1		0.1	8	1.7	-27.1	28.9	-4.1
SDP-140	113.2	0.86	0.3	7.6	2.1	-28	30.2	-5.2
SDP-138	111.7	1.61	0.1	8.2	2.3	-27	29.3	-6.7
SDP-135	110.5	2.07	0.3	9.6	2.6	-27.7	30.3	-6.6
SDP-134	109.8	0.94	0.1	6.9	0.9	-26.6	27.5	-5
SDP-132	108.6	0.7	0.2	7.2	1.7	-25.4	27.1	-4.3
SDP-131	108.4		0.1	8.2	1.4	-27	28.3	-4.4
SDP-130	108	0.76	0.2	8	0.5	-26.9	27.4	-3.8
SDP-129	107.4	0.84	0.2	7.8	1.7	-26.2	28	-4.8
SDP-128	106.7	0.89	0.2	7.1	1.9	-26.8	28.7	-4.8
SDP-126	106	1.1	0.1	8.2	2.1	-25.4	27.5	-4.7
SDP-125	105.1	1.48	0.1	6.9	2	-25.9	27.9	-5.6
SDP-124	104.7		0.1	7.4	2.5	-25.9	28.4	-4.4
SDP-123	104.2	1.48	0.2	7.4	2.3	-25.4	27.7	-5.2
SDP-122	103.2		0.2	8.9	2.6	-26.3	28.9	-4.6
SDP-121	103	1.17	0.1	8.2	2.9	-26	28.9	-5.2
SDP-120	102.2		0.3	6.7	1.9	-27.6	29.5	-4.4
SDP-119	101.3	0.71	0.2	7.5	1.5	-26.9	28.4	-4.4
SDP-118	100.5		0.2	8.3	2.3	-26.5	28.7	-4.6
SDP-117	99.5	0.4	0.2	9.7	0.9	-27.1	27.9	-6.2
SDP-116	98.8		0.2	9.5	1.6	-26.8	28.4	-4.8
SDP-114	97.7	0.93	0.1	9.4	1.8	-26.7	28.5	-4.4
SDP-111	96.4		0.1	7.6	1.7	-26.6	28.3	-5.2
SDP-110	96.1	1.39	0.2	8.6	2.1	-26.6	28.6	-4.9
SDP-108	93.3		0.1	10.5	1.8	-27.1	28.9	-5.6
SDP-106	92.1	0.16	0.1	9.6	1.5	-27.4	28.9	-6.5
SDP-103	90.7	0.16	0.1	8.7	2.1	-26.2	28.3	-7.3
SDP-101	89.7	0.17	0.1	9.2	2.1	-26.8	28.9	-7.3
SDP-99	89		0.1	8.7	2.2	-26.6	28.8	-6.7
SDP-97	87.7	0.22	0.1	7.7	1.2	-26.2	27.5	-8.1
SDP-96	87		0.1	7	1.2	-26.4	27.7	-5.7
SDP-95	86.2	0.18	0.2	7.7	1.8	-26.2	28	-5.7
SDP-94	85.4		0.1	10.8	0.1	-27.5	27.5	-4.7
SDP-92	84.5	0.45	0.4	8.4	1.4	-28.2	29.6	-6.5
SDP-91	84		0.1	10.8	1.2	-27.8	29	-7.8
SDP-89	82.7	0.48	0.2	9.7	2.7	-27.7	30.4	-7.3
SDP-88	81.9		0.2	10.4	4	-26.9	30.9	-7.3

SDP-86	80.7	0.3	0.2	8.9	4.3	-27	31.3	-7.4
SDP-84	79.2		0.2	9.6	4.5	-26.8	31.3	-8.3
SDP-83	78.6	0.32	0.3	6.9	4.3	-27.1	31.4	-9
SDP-82	77.6		0.3	8.7	4.4	-26.8	31.2	-7.9
SDP-81	76.8	0.54	0.1	11.4	4.5	-32.2	36.7	-8
SDP-80	75.4		0.2	8.5	4.7	-26.7	31.4	-7.1
SDP-78	74.2	0.58	0.3	8.6	4.6	-27	31.6	-7.7
SDP-76	73.5		0.1	11.7	4.6	-27.5	32.2	-7.7
SDP-74	72.3	1.2	0.2	11.4	3.7	-26.9	30.7	-7.8
SDP-72	70.5		0	10.4	-1.4	-26.6	25.2	-6.9
SDP-69	70.1		0.1	10.1	-1.8	-28.4	26.6	-7
SDP-67	69.4	2.21	0.2	9.5	0.6	-28.2	28.8	-7.7
SDP-71	68.7		0	11.9	1.1	-27.4	28.5	-7.5
SDP-70	67.8	0.72	0.1	11.3		-27.1		
SDP-66	66.9		0.1	11.2	3.7	-28.7	32.3	-8
SDP-64	66.2	2.21	0.1	10.7	3.4	-27.9	31.4	-8.4
SDP-62	65.3		0.1	11	3.3	-27.9	31.2	-8.1
SDP-61	64.7	1.81	0.3	11	3.2	-28.9	32.1	-7.8
SDP-60	63.4		0.3	11.7	3.6	-26.8	30.3	-8.1
SDP-59	62.7	0.71	1.2	0.6	1.4	-30	31.4	
SDP-58	62.2		0.4	1.7	2.7	-29	31.7	-8.7
SDP-57	61.6				3.3			-7.6
SDP-56	60.6				3.6			-7.6
SDP-55	59.1				4.1	-27	31.1	-8
SDP-54	58.6				3.8			-8.4
SDP-53	58.2	1.89	0.2	11.9	3.5	-28.8	32.3	-8.6
SDP-53	58.2				3.5	-28.8	32.3	-8.5
SDP-51	55.2				3.8	-27.2	31	-6.5
SDP-50	51.7				3.6	-27.7	31.4	-7.4
SDP-49	50.2				3.6			-7.2
SDP-48	47.5				3.7	-28.4	32	-7.8
SDP-47	45.2				3.9			-7.7
SDP-46	43.2				3.6	-28.3	31.9	-7.9
SDP-45	41.4				4.1	-28.8	32.9	-8.1
SDP-44	41		0.3	10.2	3.9	-27.9	31.8	-8.9
SDP-43	40.2	1.93			5.1			-8.4
SDP-42	39.2	1.63	0.2	7.8	5.5	-25.7	31.2	-8.1
SDP-41	35.2		0.1	12.3	2.8	-25.8	28.6	-7.2
SDP-40	34.4	2.57	0.2	11.6	2.8	-27.6	30.4	-8.3
SDP-39	33.5		0.2	11.1	3.2	-27.8	30.9	-8.2
SDP-38	32.4	5.63	0.1	12.1	2.1	-28.3	30.4	-8.1
SDP-37	31.6		0.3	9.9	1.5	-28.5	30	-8.9
SDP-36	31.1	6.08	0.1	10.7	2.3	-27.5	29.8	-8.8
SDP-35	23.7		0.4	7.5	2.5	-28.4	30.9	-5
SDP-34	23.1		0.6	7.3	2.8	-28.6	31.3	-5.3

SDP-33	20.9	1.23	0.6	6.7	2.8	-28.5	31.3	-4.7
SDP-32	19.9		1.2	6.1	2.6	-29.1	31.7	-3.5
SDP-31	15.9	13.64	0.5	7.2	-0.4	-28.9	28.5	-4.1
SDP-30	14.9		0.1	7.4	0.3	-27.4	27.7	-6.1
SDP-29	13.9	22.14	0.2	8	0.1	-28.9	29	-6.5
SDP-28	13.1		0.3	6.2	0.6	-31.8	32.4	-6
SDP-27	12.1	14.61	0.2	6.9	-0.3	-29.2	28.9	-7.1
SDP-8	12		0.6		1.4	-28.1	29.5	-5.8
S-11.7	11.7		0.1			-27.6		
SDP-26	11.6		0.1	0.4	-3.5	-28.4	24.9	
S-11.6	11.6		0.2			-28.8		
SDP-7	11.5		1.5		1.5	-29.5	31	-1.8
SD-40	11.3		0.5		1.5	-28.7	30.2	-3
SDP-6	11.3		0.9		1.6	-29.1	30.7	-2.6
SD-39	11		0.5		1.2	-29.2	30.5	-4.4
SDP-25	10.8	4.55	0.1	0.2	-7.3	-28	20.7	
S-10.8	10.8		0.3		1	-26.1	27.1	-2.4
SD-38(O)	10.8		0.2			-27.3		
S-10.7	10.7		0.3		1.1	-27.5	28.6	-11.5
SD-38	10.5		0.3		0.2	-28.5	28.7	-3.4
S-10.4	10.4		0.2		-0.3	-26.8	26.5	-11
SD-37	10.3		0.3		0.6	-27.4	28	-4.9
S-10.2	10.2		0.3			-29.7		
SD-36	10		0.3		1.5	-28	29.5	-5.6
S-9.9	9.9		0.2			-29.8		
SD-35	9.8		0.2		0.7	-28.6	29.3	-4.7
SD-34	9.5		0.2		-0.1	-29.9	29.7	-7.8
SD-32	9.4		0.2		0.8	-28.1	28.9	-5.3
S-9.2	9.2		0.9			-28.5		
SD-31	9.1		1.5		-2	-29.4	27.4	-10.9
S-9.0	9		3.2			-33.5		
SD-30	8.9		2.6		-2.3	-33.2	30.9	-6.5
S-8.8	8.8		3.3			-33		
SDP-5	8.7		5			-33.3		
S-8.6	8.6		4.1			-33		
SDP-4	8.5		3.1			-33.7		
S-8.4	8.4		4.3			-33.1		
SDP-23	8.2		0.3	0.5	-1	-30.1	29.2	
S-8.2	8.2		3.6			-33.4		
SDP-3	8.2		2.4			-33.6		
S-8.0	8		3.5			-33.8		
S-7.8	7.8		4.5			-33.9		
S-7.6	7.6		3.4			-33.9		
SDP-22	7.5		3.7	0.1		-33		
S-7.4	7.4		3.3			-34		

S-7.2	7.2		2.6			-33.7		
S-7.03	7		3.8			-34.2		
S-7.0	7		2.7			-34		
S-6.8	6.8		2		-3.8	-33.8	30	-8.5
S-6.6	6.6		1.3			-33.7		
S-6.4	6.4		0.2		-4.6	-33.6	29.1	-8.7
SDP-21	6.3		2	0.1		-33.5		
SDP-2	6.3		1.1			-33.3		
S-6.2	6.2		1.9			-34		
S-6.1	6.1		2.2			-34.2		
S-5.9	5.9		1.5		-3.5	-34.1	30.6	-8.6
SDP-1	5.9		1.6			-34.4		
S-5.8	5.8		2.3		-5.4	-34.2	28.8	-12.2
S-5.7	5.7		1		-3.8	-33.8	30	-8.5
S-5.5	5.5		0.8			-33.2		
S-5.4	5.4		0.1		-4	-31.3	27.3	-8.6
S-5.3	5.3		0.2		-3.9	-31.8	27.8	-8.7
S-5.25	5.3		1.3		-4.1	-34	29.8	-8
S-5.15	5.2		1		-4.7	-33.5	28.8	-8.3
S-5.05	5.1		0.1		-4.2	-29.4	25.1	-4.4
S-5.0	5		0.2		-4.2	-31.1	26.9	-8.4
SDP-20	4.8		0.1	10.8	-3.9	-32.6	28.6	-8.3
S-4.8	4.8		0.1		-3.3	-27.1	23.8	-9.5
SDP-19	4.6	3.08	1.2	0		-33.7		
S-4.5	4.5				-3.9			-8.3
SD-19	4.5		0.1		-3.9	-27.2	23.3	-8.1
SDP-18	4.5		0.1	9.1	-4.1	-30.9	26.8	-8.4
S-4.4	4.4		0.1		-4.1	-26	22	-8.3
SD-18	4.4		0.1		-3.7	-27.5	23.7	-8
S-4.3	4.3		0.1		-4.1	-25.9	21.9	-8.5
S-4.2	4.2		0.1		-4	-27.4	23.4	-8.4
SD-17	4.2		0.1		-3.9	-28	24.1	-7.9
S-4.1	4.1		0.1		-3.3	-25.8	22.5	-7.5
SD-16	4.1		0.1		-3.8	-25.3	21.5	-7.8
S-4.0	4		0.1		-3.2	-26	22.8	-7.9
SD-15	3.9		0.1		-3.4	-25.4	22	-7.5
S-3.7	3.7		0.1		-3.2	-26.6	23.3	-7.9
SD-14	3.7				-3.2			-6.8
SD-13	3.5				-2.9			-7.3
S-3.4	3.4				-3.2			-9.1
S-3.25	3.3		0.1		-3.1	-25.7	22.6	-7.5
SD-12	3.2				-3			-7.5
S-3.0	3		0.1		-3.3	-25.8	22.5	-8.1
SD-11	2.9				-2.7			-8.3
S-2.8	2.8				-3.1			-8.4

S-2.7	2.7	0.1		-26.3		
SD-10	2.7	0.2	-2.7	-27.3	24.6	-7.6
S-2.6	2.6	0.1	-2.9	-26.1	23.2	-8.5
S-2.4	2.4	0.1	-3	-26.6	23.6	-8.4
SD-9	2.4	0.3	-2.8	-26.4	23.5	-7.8
S-2.2	2.2	0.1	-2.7	-27	24.4	-8.1
SD-8	2.1	0.1	-2.9	-26.5	23.6	-7.5
S-2.0	2	0.1	-3.1	-26.5	23.3	-7.6
S-1.9	1.9		-2.7			-7.9
SD-7	1.9	0.1	-3	-26.1	23.1	-7.7
S-1.8	1.8	0.1	-3	-25.4	22.4	-8.7
S-1.6	1.6	0.1	-2.5	-26.2	23.7	-7.3
SD-6	1.5	0.1	-2.5	-25.2	22.7	-7
S-1.4	1.4	0.1	-3	-27.6	24.5	-7.9
SD-5	1.3		-2.3			-8.3
SD-4	1.2		-2.5			-7.6
S-1.1	1.1	0.1	-2.6	-26.3	23.7	-7.8
S-1.02	1	0.1	-2.9	-27.6	24.7	-7.1
S-1.0	1	0.1	-2.8	-28.1	25.3	-7.6
SD-3	0.8		-2.3			-12.4
S-0.5	0.5		-2.4	-26.1	23.8	-9.3
SD-2	0.5		-2.2			-7.8
SD-1	0.2	0.1	-2.2	-25.2	23	-7.6
S-0.1	0.1	0.1	-3	-25.8	22.8	-6.4

Note: (1) Zhangcunping section: all data are from this study; (2) Jiulongwan section: data of samples labeled with "JLW" are from this study while the rest data are from Li et al. (2010); data in McFadden et al. (2008) were not included because of their slightly different depth-scaling system from ours. (3) Siduping section: isotope data for 0-12m except samples "SDP-18 to 27" were extracted from Jiang et al. (2010) while the rest data are from this study. The C-isotope data of the Siduping section in Wang et al. (2016) were not compiled into this dataset because this dataset shows similar stratigraphic variation to ours but have different stratigraphic depth framework from ours which makes it difficult to combine them together.

REFERENCES

Jiang G, Wang X, Shi X, Zhang S (2010) Organic carbon isotope constraints on the dissolved organic carbon (DOC) reservoir at the Cryogenian-Ediacaran transition. *Earth and Planetary Science Letters* **299,** 159–168.

Li C, Love GD, Lyons TW, Fike DA, Sessions AL, Chu X (2010) A stratified redox model for the Ediacaran ocean. *Science* **328**, 80–83.

McFadden KA, Huang J, Chu XL, Jiang GQ, Kaufman AJ, Zhou CM, Yuan XL, Xiao SH (2008) Pulsed oxidation and bioloical evolution in the Ediacaran Doushantuo Formation. *Proceedings of the National Academy of Sciences of the United States of America* **105,** 3197–3202.

Wang X, Jiang G, Shi X, Xiao S (2016) Paired carbonate and organic carbon isotope variations of the Ediacaran Doushantuo Formation from an upper slope section at Siduping, South China. *Precambrian Research*, **273**, 53-66.